Delineating the Effects of Counterions on the Structural and Vibrational Properties of U(IV) Lindqvist Polyoxometalate Complexes

Primadi J. Subintoro[1] and Korey P. Carter[1*]
[1]Department of Chemistry, University of Iowa, Iowa City, IA 52242, United States

Abstract

Molecular spin qubits based on molecules that feature accessible atomic clock transitions have demonstrated immense potential in quantum information science research, and exemplary in this regard is the holmium polyoxometalate, $[Na_9Ho(W_5O_{18})_2]\bullet 35H_2O$ (HoW_{10}). The coherence time of this molecule is limited by spin-phonon coupling driven decoherence processes, and one route to overcome this limitation is to increase the magnetic anisotropy of the metal included within the polyoxometalate (POM) complex. Herein we conducted a full investigation into the fundamental structural and vibrational properties of Lindqvist POMs that include uranium (IV), which also feature $M_J = \pm 4$ ground states, similar to Ho(III) in HoW_{10}. Based on recent results from our group that demonstrated the importance of the secondary lattice elements in tuning the distortion of the D_{4d} symmetry in W_{10} POM complexes, we synthesized eight UW_{10} complexes with different alkali metal counterions and evaluated how the composition and packing of counterion species affected complex structural and vibrational properties Single crystal X-ray diffraction analysis on complexes **1-8** revealed changes in structural distortion parameters, i.e., skew angle, plane angle, and plane distance, as a function of differences in counterion configurations. Far-infrared and Raman spectra for **1-8** also demonstrated that vibrational mode frequencies [$\nu(WO_5)_2$, $\rho(UO_8)$, $\nu/\rho(UO_8)$, $\delta/\rho(UO_4)$, POM deformation mode, δ(W-O-W/W=O/U-O-W), ν(W-O-W), and ν(U-O-W)] were sensitive to changes in counterion composition and packing. To more effectively compare different counterions configuration we developed counterion effective ionic radius (eIR) as a new structural parameter and comparisons between structural distortion parameters and counterion eIR strongly suggest modulation by the secondary lattice elements can affect structural and vibrational manifolds within POM complexes. Partial Least Squares (PLS) analysis was used to quantitatively evaluate correlations observed within this investigation, and PLS statistical models showed strong correlation between counterion eIR and both structural distortion parameters and vibrational mode frequencies. Overall, this investigation illustrates how to diversify the composition of lattice elements within UW_{10} complexes and confirms the integral role counterions play in modulating the structural and vibrational characteristics of Lindqvist POM complexes with f-elements.

Introduction

Polyoxometalates (POMs) are metallic oxide materials formed by MO_6 octahedral moieties of primarily group V and VI metals (V, Nb, Ta, Mo, and W) that are connected through bridging oxygen atoms to form discrete structures.[1, 2] This class of materials is continuously relevant due to their topological diversity and modularity, which allow for unique electronic properties to be realized both in the POM and for the metals that POMs encapsulate.[3, 4] Evidence of the potential of POMs can be seen through the wide range of applications where POMs have been used including catalysis, medical contrast agents, and, more recently, quantum information science (QIS).[5-9] POMs are known to form stable complexes with highly oxophilic cations such as f-block elements, and this is especially true for lacunary POMs wherein vacancies in MO_6 units are generated, thereby increasing the basicity of the remaining bridging oxygens atoms.[2] The diverse array of known lacunary POM species provides a pathway to generate f-element coordination complexes with a range of unique topologies,[10] and notables examples with lanthanide cations include sandwich complexes with lacunary Lindqvist, Keggin, and Wells-Dawson POMs.[11-15] More recently, lacunary POMs have also been documented to successfully chelate microgram quantities of Am(III) and Cm(III), which highlights the translatability of POM chemistry towards the actinides.[16-18] Beyond providing a platform to study metal-ligand bonding with rare transplutonium elements, POM chemistry has also been investigated with early actinides including thorium, uranium, and neptunium.[19-23]

Actinide POM chemistry has been an area of sustained research interest since the 1970s as this class of complexes was initially investigated for the separation and storage of radioactive elements,[24] and current efforts have evolved to take advantage of the rich redox and spin-based properties exhibited by actinide complexes.[25, 26] The advent of high-performance molecular magnets based on Ln(III) cations, such as Dy(III) and Tb(III), is one new avenue for exploration, especially as theoretical calculations on uranium (III) and U(V) molecular magnets suggest that these systems should be able to eclipse the performance of their lanthanide counterparts, although experimental results have thus far shown otherwise.[25, 27, 28] The challenge in realizing actinide single molecule magnets is not a limiting factor for other applications that can take advantage of the unique spin-based properties of the 5f elements, such as QIS where actinide complexes could function as electron spin quantum bits (qubits). Molecular spintronic materials, especially spin qubits, are often paramagnetic metal complexes wherein a two-level system can be generated via application of a magnetic field.[29-31] A key metric for assessing spin qubits is the coherence time of a species, which is a measure of the length of time spins spend in the superposition state of the two spin-levels. Baldovi *et al*. have predicted that a U(IV) molecule with a stabilized $M_J = \pm 4$ ground state could feature a large tunnel splitting gap akin to the one exhibited by the model spin qubit, $Na_9Ho(W_5O_{18})_2 \cdot 35H_2O$ (HoW_{10}),[32, 33] and realization of this property in a U(IV) POM could lead to an extremely long coherence time via an accessible atomic clock transition. Inspired by the work of Shiddiq and colleagues who detailed that HoW_{10} could act as a spin qubit, as well as our recent study that elucidated the role of structural polymorphism and second sphere interactions on vibrational properties of lanthanide Lindqvist POM complexes,[15, 33] we have extended our investigations into POM chemistry to the $[U(IV)(W_5O_{18})_2]^{8-}$ (UW_{10}) system. The distorted square antiprismatic (D_{4d}) symmetry that results from formation of a sandwich complex with lacunary Lindqvist POMs stabilizes the ± 4 M_J states of the Ho(III) cation in HoW_{10}, and our hypothesis here is that the same outcome can be achieved for the non-Kramers U(IV) ion, which also possesses a $M_J = \pm 4$ ground state.

Herein we investigated the structural and vibrational properties of UW_{10} complexes with each of the alkali metals acting as charge balancing counterions. Despite its fundamental importance in actinide POM chemistry, there has not been a study that elucidates the fundamental properties of UW_{10} complexes since the first synthesis procedure for this molecule was published five decades ago by Golubev *et al*.[34] In our recent work focused on $Na_9Ln(W_5O_{18})_2 \cdot XH_2O$ complexes we found that the secondary lattice influenced the effective symmetry of the Ln(III) center through the distortion of the D_{4d} symmetry which affected both the vibrational and spin manifolds of the complexes. Colliard and Deblonde have also noted direct ion pairing interactions with POM clusters and actinide metal centers in their recent studies focused on transplutonium POMs where Cs(I) has been used as a counterion.[18] Here we aimed to develop a more comprehensive understanding of the role of counterions on the second sphere interactions in POM complexes by synthesizing UW_{10} complexes with combinations of Na(I) and each of the other alkali metals acting act as charge balancing cations. Further, we also prepared UW_{10} complexes with only Li(I), K(I), or Cs(I) counterions to investigate whether and to what extent the effective symmetry of a metal center be tuned by controlling the composition of counterions within the secondary sphere. Overall, eight species of UW_{10} ($Li_5Na_3[UW_{10}]$ (**1**), $Na_8[UW_{10}]$ (**2**), $K_4Na_4[UW_{10}]$ (**3**), $Rb_6Na_2[UW_{10}]$ (**4**), $Cs_{5.5}Na_{2.5}[UW_{10}]$ (**5**), $Li_8[UW_{10}]$ (**6**), $K_8[UW_{10}]$ (**7**), and $Cs_8[UW_{10}]$ (**8**)) were synthesized and characterized structurally using X-ray diffraction and vibrationally using Raman, mid-infrared (MIR), and far-infrared (FIR) spectroscopies. Structural analyses of complexes **1**-**8** shows that larger counterions (K(I), Rb(I), and Cs(I)) participate in more ion-pairing interactions with the cluster compared to smaller counterions (Li(I) and Na(I)). Manifestations of these differences in secondary sphere interactions are significant as the effective symmetry of U(IV) metal center is modulated, which we quantifiably probed using partial least squares (PLS) analysis. Qualitative and PLS analyses of structural and vibrational properties of complexes **1**-**8** also show correlations between the identity of secondary sphere cations and shifts in Raman and IR stretching

frequencies. With this study, we aim to reinvigorate the interest in the UW_{10} species as it could be a model complex for actinide QIS applications based on its relevant symmetry for magnetic and spintronic purposes as well as a template for extending POM chemistry to tetravalent transuranic systems.

Materials and Methods

Caution! ^{238}U ($t_{1/2} = 4.47 \times 10^9$ years) is an α-emitting radionuclide that should be manipulated only in a specifically designated facility in accordance with appropriate safety controls. All measurements were taken either in the University of Iowa radiological laboratories and/or using multiple containment procedures.

Materials. All chemicals were purchased from commercial vendors and were used as received. This includes uranyl nitrate hexahydrate ($UO_2(NO_3)_2$•$6H_2O$) (International Bioanalytical Industries, 98%), hexachloropropene (C_3Cl_6) (Sigma-Aldrich, ≥90%), sodium tungstate dihydrate (Na_2WO_4•$2H_2O$) (Strem Chemicals, Inc., 99+%), potassium tungstate (K_2WO_4) (Beantown Chemical, 99.5%), cesium tungstate (Cs_2WO_4) (Beantown Chemical, 99.9%), lithium chloride (LiCl) (Strem Chemicals, Inc., 99%), sodium chloride (NaCl) (Fisher Scientific, 99%), potassium chloride (KCl) (VWR BDH Chemicals, 99%), rubidium chloride (RbCl) (Ambeed Inc., 99%), cesium chloride (CsCl) (TCI America, 99%), sodium hydroxide pellets (Fisher Scientific, ACS grade), and 70% nitric acid (Sigma Aldrich or Fisher Scientific, ACS reagent).

Experimental Methods

Synthesis of UCl_4. The method used here for preparing UCl_4 was adapted from Liddle *et al*. and Hermann and Suttle.[35, 36] 1.4779 grams of uranyl nitrate hexahydrate ($UO_2(NO_3)_2$•$6H_2O$) (~3 mmol) and 12 mL of hexachloropropene (C_3Cl_6) were added into a 50 mL round bottom flask equipped with a reflux condenser. The suspension was then refluxed at 210 ºC for approximately twelve hours. The solid $UO_2(NO_3)_2$•$6H_2O$ dissolved into the solution at 180 ºC turning it brown in color. Brown fumes were produced at temperatures above 180 ºC followed by white fumes at temperatures above 200 ºC. At 210 ºC, dark green precipitate formed, and the brown solution darkened. After twelve hours, the solution was cooled down and the solution was transferred to a 15 mL centrifuge tube with a minimal amount (~5 mL) of dichloromethane (DCM). The solution was then centrifuged at 7830 rpm for two minutes and the supernatant liquid was removed. A dark green pellet remained, and it was washed with DCM three times and dried in a vacuum desiccator for approximately three hours. The dark green solid was UCl_4 (yield = 1.1856 grams, 106.11 %), and the greater than 100% yield was due to residual DCM. This impurity did not impact subsequent POM synthesis, so the UCl_4 product was dissolved in 20 mL of 2 M hydrochloric acid, and remaining solids were removed by centrifugation. The final UCl_4 concentration was approximately 0.15 M, and this stock solution was stored in a 5 ºC fridge to maintain uranium oxidation state stability in between reactions.

Synthesis of $M_{8-x}Na_x[U(W_5O_{18})_2]$•$YH_2O$ (M = Li (1), Na (2), K (3), Rb (4), Cs (5)) and $M_8[U(W_5O_{18})_2]$•XH_2O (M = Li (6)). Synthesis of UW_{10} complexes used a procedure adapted from the work of Mariichak and colleagues.[37] 20 mL of 0.5 M Na_2WO_4•$2H_2O$ solution (10 mmol) and 0.51 mL of concentrated HNO_3 (~8 mmol) was mixed in a 100 mL round bottom flask with vigorous stirring (pH = 7.4). 6.667 mL of 0.15 M UCl_4 solution was added into the acidified tungstate solution (pH = 0.10) in 500 µL portions every 30 seconds. 3.333 mL of 4 M NaOH was then added to readjust the pH to 6.7 and 19.49 mL Milli-Q H_2O was added to yield a final volume of 50 mL. This solution was split equally into five vials and then 6.667 mL of the respective alkali metal chloride stock solution, either 2 M LiCl, KCl, RbCl, or CsCl (13.332 mmol), was added except for complex **2** where Na(I) ions in the reaction solution from Na_2WO_4•$2H_2O$ and NaOH provided a sufficient concentration of this counterion. UW_{10} solutions were stirred for fifteen minutes and then each was centrifuged for five minutes at 7830 rpm. Supernatant solutions were then collected and left to slowly evaporate in plastic petri dishes inside a 5 ºC fridge. During this slow evaporation period, small amounts of white precipitate formed in each reaction, and these precipitates were removed via centrifugation at 5 ºC. Supernatant solutions were extracted and left to slowly evaporate again until dark brown crystals formed after approximately three days. Worthy of additional comment, complexes

2-5 are indefinitely stable upon crystallization while complex **6** was isolated from the first round of crystallization of the synthesis of complex **1**. Subsequently, complex **1** can be isolated; however, this species also breaks down into complex **2** after several rounds of recrystallization, which is a likely result of the Li(I) ions being mobile within the lattice due to a lack of association interactions with the UW_{10} POM complex.

Synthesis of $M_8[U(W_5O_{18})_2]\bullet XH_2O$ (M = K (7), Cs (8)). 204 mg of K_2WO_4 (0.625 mmol) was dissolved in 5 mL of Milli-Q H_2O. The pH of the tungstate solution was raised to approximately 12 with 4 M KOH, and then the tungstate solution was acidified to a pH of 6.5 – 7 with concentrated HNO_3. 417 µL of 0.15 M UCl_4 solution was then added into the tungstate solution. The pH of the solution was readjusted back to between 6.5 and 7 with 4 M KOH solution and the solution was stirred for fifteen minutes at 60 ºC. The solution was then centrifuged, and the supernatant was extracted and left to slowly evaporate until dark brown crystals formed after approximately one week. The Cs_8 version of UW_{10} was synthesized following the same protocol outlined above for the K_8 complex with 321 mg of Cs_2WO_4 (0.625 mmol) and 2 M CsOH used instead of K_2WO_4 and KOH.

Single Crystal X-Ray Structure Determination. Single crystal X-ray diffraction data for complexes **1-8** were collected at 100(2) K on a Bruker D8 Venture Duo Diffractometer with Mo X-Ray source, $K\alpha_1$ = 0.71073 Å. Adsorption corrections were applied using the SADABS multi-scan method within the APEX4 software package.[38, 39] Structures were solved via intrinsic phasing using SHELXT and refined with SHELXL contained within Olex2 1.5.[40, 41] All non-hydrogen atoms were refined anisotropically. Due to disorder, some of the lattice counterions and water oxygen atoms were refined with less than full occupancy. ISOR restraints were also used, when necessary, on lattice atoms to yield reasonable thermal ellipsoids. Complex **4** crystallized in a non-centrosymmetric space group and the Hooft parameter from the refinement suggested the dataset was collected on a racemically twinned crystal. To account for this twinning, a racemic twin law and BASF commands were applied to the refinement, which substantively the improved crystallographic refinement metrics. Hydrogen atoms on the lattice water molecules could not be located for complexes **1-8** were not modeled. All figures for complexes **1-8** were made using CrystalMaker.[42] The packing of complexes **1-8** were determined by centering the structure on the U atoms and expanding the range until all the counterions were located. Crystallographic parameters for complexes **1-8** are available in **Table 1**. CIF files available online in the Cambridge Crystallographic Database Center (CCDC) at http://www.ccdc.cam.ac.uk by citing reference numbers 2381891 - 2381898.

Table 1. Crystallographic parameters for complexes **1-8**.

	$UW_{10}Li$ (**1**)	$UW_{10}Na$ (**2**)	$UW_{10}K$ (**3**)	$UW_{10}Rb$ (**4**)	$UW_{10}Cs$ (**5**)	$UW_{10}LiF$ (**6**)	$UW_{10}KF$ (**7**)	$UW_{10}CsF$ (**8**)
Formula	$Li_5Na_3UW_{10}O_{36}$ $\bullet 19H_2O$	$Na_8UW_{10}O_{36}$ $\bullet 31H_2O$	$K_4Na_4UW_{10}O_{36}$ $\bullet 17H_2O$	$Rb_6Na_2UW_{10}O_{36}$ $\bullet 11H_2O$	$Cs_{5.5}Na_{2.5}UW_{10}O_{36}$ $\bullet 5H_2O$	$Li_8UW_{10}O_{36}$ $\bullet 14H_2O$	$K_8UW_{10}O_{36}$ $\bullet 5H_2O$	$Cs_8UW_{10}O_{36}$ $\bullet 12H_2O$
Mr	3220.2	3332.45	3160.89	3387.33	3552.88	2932.05	3149.33	3899.81
SG	$P2_1/n$	C2/c	$P2_1/c$	Cc	Pnma	$P2_1/n$	$P2_1/n$	P-1
a(Å)	18.1042 (6)	18.0046 (8)	25.9688 (14)	9.8894 (4)	27.4711 (12)	9.2004 (3)	21.7357 (7)	10.3539 (3)
b(Å)	18.2289 (6)	18.6315 (8)	11.2067 (5)	20.0696 (9)	11.3562 (4)	29.5003 (8)	9.4184 (3)	13.1902 (5)
c(Å)	18.2154 (6)	18.4017 (7)	17.58058 (9)	26.0571 (9)	17.0364 (7)	15.2620 (6)	25.5666 (9)	19.2245 (7)
α	90	90	90	90	90	90	90	88.171 (2)
β	98.962 (1)	95.213 (2)	92.994 (2)	93.641 (2)	90	93.980 (2)	103.065 (1)	85.149 (1)
γ	90	90	90	90	90	90	90	75.357 (1)
V($Å^3$)	5938.1 (3)	6147.4 (4)	5109.4 (4)	5161.3 (4)	5314.8(4)	4132.3 (2)	5098.4 (3)	2530.96 (15)
Rint	0.0952	0.0789	0.0911	0.0779	0.0640	0.0775	0.0794	0.0719
R1	0.0336	0.0332	0.0365	0.0345	0.0574	0.0307	0.0341	0.0319
wR2	0.0763	0.0921	0.0829	0.0813	0.1631	0.0657	0.0803	0.0622
GooF	1.134	1.313	1.067	1.078	1.173	1.065	1.078	1.124
Mu(mm^{-1})	22.147	21.434	26.043	31.051	28.404	31.744	26.38	31.584
F000	5600	5824	5480	5808	6047.0	5024	5456	3304
Z	4	4	4	4	4	4	4	2
Dx (g/cm^3)	3.602	3.601	4.109	4.359	4.455	4.713	4.103	5.117
Temp. (K)	100 (2)	100 (2)	100 (2)	100 (2)	100 (2)	100 (2)	100 (2)	100 (2)
Wavelength (Å)	0.71073	0.71073	0.71073	0.71073	0.71073	0.71073	0.71073	0.71073

Raman and Infrared (IR) spectroscopies. Raman spectra for complexes **1-8** were collected on a ReniShaw InVia Raman microscope. The spectra were collected using a 785 nm laser at varying power, 20X magnification, and the extended scan setting with a spectral window of 1500-100 cm^{-1}. The scan parameters were ten second exposure times and three scans per spectrum. Data for each sample was collected in triplicate to minimize orientation effects. The Raman spectra were standardized by dividing the raw intensity values by laser power (200 mW, 100% for 785 nm laser) and exposure time. IR spectra for complexes **1-8** were collected in both the mid-IR (MIR) (4500-400 cm^{-1}) and far-IR (FIR) (400-100 cm^{-1}) spectral windows under vacuum on a Bruker VERTEX 70V spectrometer using a platinum ATR microscope objective and the OPUS 8.5 software package. The resolution for MIR and FIR measurements are 0.4 cm^{-1} and 1 cm^{-1}, respectively. Baseline corrections on the Raman and IR data were done using the PreDICT and Origin2024 software packages, respectively. Peak fitting for both Raman and IR spectra were done in Origin2024.[43]

Partial Least Squares (PLS) Analysis. PLS analysis was done in the Origin2024 software package using the singular value decomposition (SVD) method.[43] The leave-one-out cross-validation method was also used to prevent overfitting of PLS models and to determine the number of latent variables to build into each model. PLS regression models were built for both structural distortion parameters (DPs) (skew angles, plane angles, and plane distances) and vibrational mode frequencies. The PLS analysis of the distortion parameters included unit cell parameters obtained from X-ray crystal structures (a, b, c, β, V), average d_{U-O} distances, the effective ionic radii (eIR) of the counterions, and the average d_{U-M} distances (M = Li(I), Na(I), K(I), Rb(I), Cs(I)) as independent variables and the distortion parameters as the dependent variables. PLS models built to investigate correlations between the structural parameters and vibrational mode frequencies incorporated the DPs, counterion eIR, and average d_{U-M} distances as the independent variables and the Raman or FIR mode frequencies as the dependent variables. More details regarding the PLS analysis are included in the PLS section of the **Supporting Information**.

Results and Discussion

Synthesis

UW_{10} was first synthesized and crystallographically characterized in 1975 by Golubev *et al.*;[34] however, this complex has not received any subsequent research attention since this initial study. The most widely used procedure for synthesizing $[An(IV)/Ln(III)W_{10}O_{36}]^{8/9-}$ complexes is via the Peacock and Weakley method in which a solution of sodium tungstate is acidified with glacial acetic acid until the reaction solution pH is between 6.5 and 7.5.[14] In recent work from our group focused on LnW_{10} complexes,[15] we found that this method produced a significant amount of byproducts, in the form of sodium paratungstate, and hence we used the procedure outlined by Mariichak and colleagues.[37] This method employs a strong acid such as HNO_3 or HCl as the acidifying agent, which reduces side product formation dramatically, and here we extended this procedure to an actinide system for the first time. For synthesis of **1-8**, the identity of the starting U(IV) salt is also important as attempts to use $U(SO_4)_2$ as a U(IV) source resulted in the formation of UO_2. In contrast, addition of UCl_4 into the sodium tungstate solution results in a solution color change (to brown) and the formation of a white precipitate. Since our UCl_4 stock solution was in 2 M HCl, the pH of the reaction solution needed to be adjusted back to between 6.5 and 7 with NaOH. With each addition of a NaOH aliquot, in-growth of a dark green color can be seen in the U(IV)-POM solution. The final color of the U(IV)-POM solution can be either brown or dark green depending on the final pH, and after a day the dark green solutions also turn brown. Despite the differences in reaction solution color, there are no differences in the final product as long as UCl_4 is used as the uranium source and the final reaction pH is between 6.5 – 7. After solutions are allowed to slow evaporate for three to five days, dark brown crystals of **1-6** can be found in the mother liquor. The crystals of **6** can only be isolated during the first round of crystallization from the synthesis protocol for **1** and after subsequent rounds of recrystallization crystals of **1** evolve into a new polymorph (**1b**), and eventually into complex **2**.

The synthesis of complexes **7** and **8** follows similar principles to those outlined above. Potassium and cesium tungstates along with potassium and cesium hydroxides are used instead of sodium tungstate and sodium hydroxide for the synthesis of **7** and **8**, respectively. Beside the starting materials, the only difference between the synthesis method for **1**-**6** and the protocol for **7** and **8** is the first pH adjustment step. Without an initial pH adjustment, we found these reactions to be unsuccessful, yielding none of the desired products. Upon comparing the FTIR spectra of our K_2WO_4 and Cs_2WO_4 starting materials with that of our Na_2WO_4 source, we found the sharp ν(O-W-O) peak centered at 815 cm^{-1} that is characteristically observed for Na_2WO_4 is broader and contains multiple shoulders in our K_2WO_4 and Cs_2WO_4 spectra, **Figure S1** (**Supporting Information**).[44] The FTIR spectrum of Na_2WO_4 also included stretching frequencies associated with the WO_4^{2-} tetrahedron located in the 700-400 cm^{-1} region, which are absent in the K_2WO_4 and Cs_2WO_4 MIR spectra.[44] These differences in tungstate FTIR spectra suggested that our K_2WO_4 and Cs_2WO_4 starting materials had potentially started to hydrolyze and condensate, thereby yielding unknown POM phases.[15, 37, 45-47] It is well documented that tungsten based POMs degrade under basic condition;[1, 2] hence, adjusting reaction solutions to higher pH values ensured that POM contaminants would break down. After basification, the synthesis protocol for **7** and **8** followed the same steps that were used to produce complexes **1**-**6**.

Single Crystal X-ray Structure Descriptions

Single crystal X-ray diffraction data analysis revealed that complexes **1** and **3**-**8** are new structures, while complex **2** matched the previously reported structure from Golubev *et al*.[34] Complexes **1**-**8** crystallized in seven different space groups, specifically complexes **1** ($Li_5Na_3[UW_{10}]$) and **6** ($Li_8[UW_{10}]$) in $P2_1/n$, complex **2** ($Na_8[UW_{10}]$) in C2/c, complex **3** ($K_4Na_4[UW_{10}]$) in $P2_1/c$, complex **4** ($Rb_6Na_2[UW_{10}]$) in Cc, complex **5** ($Cs_{5.5}Na_{2.5}[UW_{10}]$) in Pnma, complex **7** ($K_8[UW_{10}]$) in P2/n, and complex **8** ($Cs_8[UW_{10}]$) in P-1. Throughout **1**-**8**, UW_{10} moieties remain constant with differences in structures and packing due to the location of counterions and their interactions with lattice solvent and/or the POM clusters (**Figure 1**). The UW_{10} clusters in complexes **1**-**8** are formed by two lacunary $[(W_5O_{18})^{6-}]$ (W_5) POMs that are connected by a U(IV) cation at the lacunary sites of the W_5 moieties. The U(IV) cations are coordinated by the four terminal oxygens of the lacunary sites from two W_5 POMs, which results in U(IV) coordination numbers of eight in all complexes and distorted square antiprismatic (D_{4d}) symmetry for each of the U(IV) cations. These metal-ion coordination number and point group symmetry characteristics for U(IV) match what we observed for Ln(III) cations in the LnW_{10} series,[15] and average distances between the coordinating oxygens and U(IV) cations ($d_{U\text{-}O}$) are 2.371 Å, 2.369 Å, 2.368 Å, 2.371 Å, 2.365 Å, 2.367 Å, 2.371 Å, and 2.361 Å for complexes **1**-**8**, respectively.

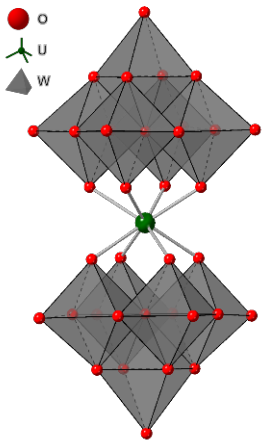

Figure 1. Polyhedral representation of the $[U(W_5O_{18})_2]^{8-}$ (UW_{10}) moiety.

The two primary packing configurations observed in complexes **1-8** are highlighted in **Figure 2**. As counterions impact the vibrational and spin manifolds of f-element POMs, each asymmetric unit for complexes **1-8** will be described in detail and interatomic distances that are discussed in this section are compiled in **Table S1** (**Supporting Information**). The asymmetric unit of **1**, **Figure S2** (**Supporting Information**), includes one UW_{10} moiety, five Li(I) ions, and three Na(I) ions, and not all counterion sites are fully occupied, which indicates that there is significant disorder in the lattice. Li(I) cations are coordinated by four lattice water molecules and adopt tetrahedral coordination environments, whereas Na(I) cations are coordinated by six lattice water molecules in octahedral coordination environments. The packing of **1** shows **Na2** and **Na3** directly interacting with the terminal oxygens of the UW_{10} subunits via **O11** ($d_{Na2\text{-}O11}$ = 2.447 Å) and **O25** ($d_{Na3\text{-}O25}$ = 2.421 Å), respectively. On the other hand, there are less interactions between the Li(I) cations with the POM cluster despite the higher abundance of Li(I) compared to Na(I) in the lattice, with only **Li5** directly interacting with the cluster moiety through **O9** ($d_{Li5\text{-}O9}$ = 2.369 Å). Interestingly, the closest distance between Li(I) and U(IV) atoms ($d_{U\text{-}Li}$) is shorter than the closest distance between a Na(I) atom and the U(IV) metal center ($d_{U\text{-}Na}$) with values of 5.613 Å (**U1-Li3**) and 5.837 Å (**U1-Na1**), respectively. However, the average distance between Li(I) cations and U(IV) cations (avg $d_{U\text{-}Li}$ = 6.412 Å) is longer than the average distance between Na(I) cations and U(IV) cations (avg $d_{U\text{-}Na}$ = 6.358 Å). Complex **1**, $Li_5Na_3[UW_{10}]$, evolves after several rounds of re-crystallization to form another polymorph of $UW_{10}Li$ (**1b**) and eventually breaks down into complex **2**. Complex **1b** has a completely different set of crystallographic parameters than **1**, **Table S2 (Supporting Information)**, and it turns out to be the more stable polymorph as we often obtained complex **1b** when attempting to synthesize complex **1**. Unfortunately, the crystallography involving **1b** is very challenging and only a unit cell for this complex could be acquired despite the pristine physical morphology of the crystals, **Figure S3 (Supporting Information)**. The source of disorder for **1b** might be the lack of association between the Li(I) cations and the UW_{10} cluster, which would allow for more freedom of movement for the Li(I) cations within the lattice, and the evolution of complexes of **1**/**1b** to **2** is probably a result of the thermodynamic instabilities that result from the transient nature of Li(I) interactions with POM clusters and lattice water molecules.[48]

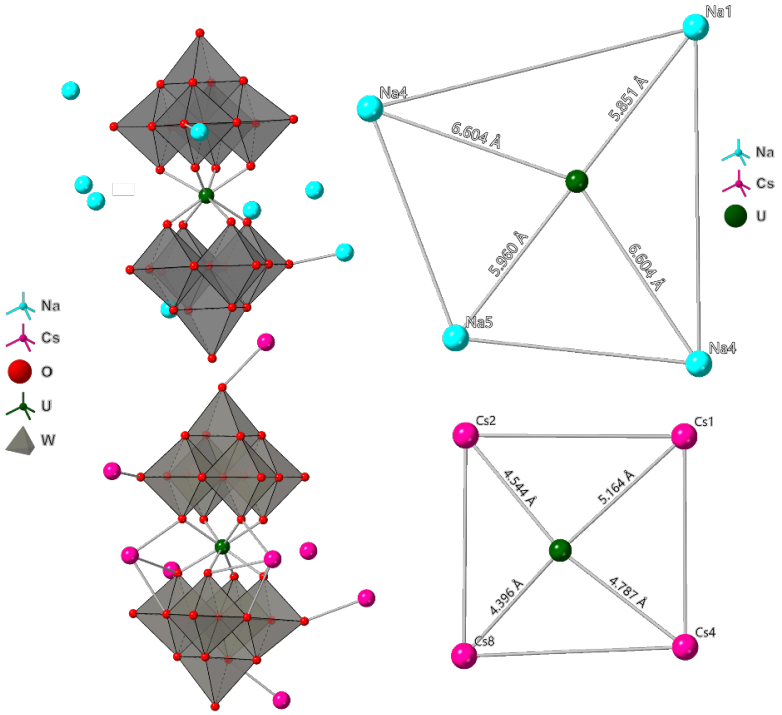

Figure 2. (**Left**) Polyhedral representations of complexes **2** and **8**. Oxygen atoms from lattice water molecules were excluded for clarity. (**Right**) Ball and stick representation of the UW_{10} belt area (boxed) for **2** and **8**. Complexes **2** and **8** serve as representative examples for species with lighter and heavier counterions, respectively. The heavier Cs(I) ions in **8** are located closer to the cluster compared to the Na(I) ions in **2** indicating a preference for ion-pairing interactions between the Cs(I) ions and the UW_{10} cluster.

Complex **2** is the only species with precedent in the literature, yet no description of the structure or details on the packing of the lattice are included in the work of Golubev *et al*.[34] The asymmetric unit of **2**, **Figure S4** (**Supporting Information**), contains half of a UW_{10} moiety and five unique Na(I) cations. The U(IV) cation (**U1**) along with two Na(I) cations (**Na1** and **Na5**) sit on crystallographic special positions with half occupancy. The Na(I) cations adopt octahedral coordination environments via interactions with lattice water molecules or cluster oxygen atoms. All the Na(I) cations form a network with lattice water molecules that is localized in one region of the asymmetric unit, and there are direct interactions with the POM cluster via oxygen atom **O9** which interacts with **Na2** ($d_{Na2\text{-}O9}$ = 2.505 Å). The closest Na(I)-U(IV) distance ($d_{U\text{-}Na}$) for **2** is 5.851 Å (**U1-Na1**) and the average $d_{U\text{-}Na}$ distance is 6.494 Å. Comparing **2** with other tetravalent f-element analogues, specifically $Na_8[Ce(IV)W_{10}]$ and $Na_8[Th(IV)W_{10}]$, the Na(I) cations occupy identical positions with similar closest Na(I)-M(IV) distances of 5.852 Å ($d_{Ce(IV)\text{-}Na}$) and 5.863 Å ($d_{Th\text{-}Na}$), respectively, **Figure S4** (**Supporting Information**).

The asymmetric unit of **3**, **Figure S5** (**Supporting Information**), contains a full UW_{10} moiety, four Na(I) cations, and four K(I) cations. The typical coordination number for K(I) cations is eight to ten and this is matched by the coordination environment of the K(I) cations (CNs = 8 and 9) here.[49] **K1** and **K3** exhibit coordination numbers of nine and these expanded coordination environments are a likely result of interactions with multiple UW_{10} moieties. Inspection of the packing for **3** reveals that all K(I) cations interact directly with the UW_{10} moiety. **K1** and **K4** atoms participate in ion-pairing interactions with the cluster via oxygen atoms **O11** ($d_{K1\text{-}O11}$ = 2.738 Å) and **O18** ($d_{K4\text{-}O18}$ = 2.767 Å). The potassium cations **K2** and **K3** display more extensive ion-pairing interactions with both K(I) cations interacting with multiple cluster oxygen atoms (**O2**, **O19**, **O20**, and **O26** for **K2** (average $d_{K2\text{-}O}$ = 2.934 Å); **O24**, **O33**, and **O34** for **K3** (average $d_{K3\text{-}O}$ = 2.909 Å)). Notably, **K2** interacts with three uranium coordinating oxygens from both W_5 units, which enhances its ability to participate in direct ion-pairing interactions with the U(IV) center. This area around the U(IV) cations is designated as the belt region, and it is the region where ion-pairing interactions are expected to occur based on the recent findings from Colliard and Deblonde.[18] In contrast, the Na(I) cations in the asymmetric unit of **3** are located farther from the UW_{10} moiety and only the disordered sodium atom **Na4A/B** directly interacts with the cluster through oxygen atom **O7** (average $d_{Na4\text{-}O7}$ = 2.464 Å). The greater association between K(I) cations and the UW_{10} cluster are reflected in the closest interaction distances ($d_{U\text{-}M}$) for each of the lattice counterions, and for **3** these $d_{U\text{-}K}$ and $d_{U\text{-}Na}$ values are 4.035 Å (**U1-K2)** and 4.421 Å (**U1-Na3**). Moreover, the average $d_{U\text{-}K}$ and $d_{U\text{-}Na}$ distances also support the observation that association interactions with K(I) are stronger in complex **3** with values of 6.189 Å ($d_{U\text{-}K}$) and 6.375 Å ($d_{U\text{-}Na}$), respectively.

The asymmetric unit of complex **4**, **Figure S6** (**Supporting Information**), contains a full UW_{10} moiety, six Rb(I) cations, and two Na(I) cations. The Rb(I) cations exhibit coordination numbers ranging from four to nine, and higher coordination numbers are typical for Rb(I), whereas Rb(I) does not often have coordination numbers below six.[49] There are six unique positions for the Rb(I) cations in the asymmetric unit of **4** with **Rb1**, **Rb2**, **Rb4**, and **Rb5** located at the periphery of the UW_{10} cluster. The packing of **4** show **Rb1** interacts with the cluster through three POM oxygen atoms, **O30**, **O33** and **O34** (average $d_{Rb1\text{-}O}$ = 3.066 Å), while **Rb2** interacts with the cluster through only one oxygen atom, **O36** ($d_{Rb2\text{-}O36}$ = 2.932 Å). **Rb4** also interacts with the UW_{10} moiety through three oxygen atoms, **O6**, **O15**, and **O16** (average $d_{Rb4\text{-}O}$ = 3.115 Å), whereas the coordination behavior of **Rb5** is distinct as this counterion only interacts with the

UW_{10} moiety through **O28** ($d_{Rb5\text{-}O28}$ = 2.932 Å) and features a coordination number of five, a likely result of packing constrains that limit **Rb5** interactions with nearby UW_{10} clusters. The other Rb(I) cations in complex **4**, **Rb3** and **Rb6**, are located in the belt area of the structure and engage in direct ion-pairing interactions with the UW_{10} POM. **Rb3** interacts with the cluster through oxygen atoms **O4**, **O19**, and **O26** (average $d_{Rb3\text{-}O}$ = 2.999 Å), and overall **Rb3** adopts a coordination number of four. The neighboring **Rb6** is crystallographically disordered and structural modeling reveals electron density from this cation is split over four different positions in the belt area (**Rb6A-D**) where coordination numbers are four or five. **Rb6A** interacts with the cluster through oxygen atoms **O3**, and **O11** (average $d_{Rb6A\text{-}O}$ = 2.953 Å), **Rb6B** interacts with the cluster through oxygen atoms **O3**, **O10**, and **O21** (average $d_{Rb6B\text{-}O}$ = 2.984 Å), **Rb6C** interacts with the cluster through oxygen atoms **O2**, **O21**, and **O30** (average $d_{Rb6C\text{-}O}$ = 3.055 Å), and **Rb6D** interacts with the cluster through four oxygen atoms, **O1**, **O2**, **O8**, and **O22** (average $d_{Rb6D\text{-}O}$ = 3.101 Å). The two unique Na(I) cations in **4** are part of a water network in the lattice and do not interact directly with the UW_{10} cluster, instead participating in interactions with **Rb1** and **Rb5**. This configuration of heavier counterions being located closer to the metal POM compared to the lighter counterions is reflected in the avg $d_{U\text{-}Rb}$ distance (6.010 Å) being much shorter than the avg $d_{U\text{-}Na}$ distance (8.102 Å). The closest alkali metal-U(IV) interaction distances are 4.212 Å (**U1-Rb3**) and 7.992 Å (**U1-Na2**), respectively, which further demonstrates there are significant difference in interactions with the cluster for Rb(I) and Na(I). The increase in direct ion-pairing interactions with heavier counterions in both **3** and **4** is due to stronger electrostatic interactions between U(IV) and the alkali metal cation, and similar findings have also been noted by Colliard and Deblonde and Zagrebin *et al*. in their studies on f-element POMs.[18, 48]

The asymmetric unit of **5** contains half of a UW_{10} cluster, 2.75 Cs(I) cations, and 1.25 Na(I) cations, **Figure S7** (**Supporting Information**). There are four distinct sites for Cs(I) cations in **5** and in each location Cs(I) counterions adopt typical coordination numbers ranging from seven to nine, and notably all Cs(I) cations directly interact with the UW_{10} cluster, consistent with our observations for K(I) counterions in **3** and Rb(I) counterions in **4**. Due to the higher symmetry space group (Pnma) for **5**, many of the atoms in the structure reside on crystallographic special positions which affect their overall occupancy; however, this does not hinder our ability to discuss complex packing. **Cs1** is one of two non-disordered Cs(I) cations within the structure, and it features a coordination number of eight and interacts directly with the cluster through oxygen atoms **O18** and **O21** (average $d_{Cs1\text{-}O}$ = 3.087 Å). **Cs2** on the other hand, is disordered over three positions, **Cs2A-C**. **Cs2A** adopts a coordination number of nine and interacts with the cluster oxygens, **O2**, **O12**, **O13**, and **O18** (average $d_{CsA\text{-}O}$ = 3.260 Å), **Cs2B** has a coordination number of seven and interacts with the cluster through oxygen atoms, **O2**, **O4**, and **O13** (average $d_{Cs2B\text{-}O}$ = 3.338 Å), and **Cs2C** features coordination number of eight and interacts with cluster oxygens, **O4** and **O13** (average $d_{Cs2C\text{-}O}$ = 3.345 Å). **Cs3** is also disordered but only over two positions, **Cs3A-B**. **Cs3A** features a coordination number of seven and interacts directly with the cluster through oxygens, **O1**, **O14**, and **O16** (average $d_{Cs3A\text{-}O}$ = 3.2217 Å), whereas **Cs3B** features a coordination number of nine and interacts with cluster oxygens, **O1** and **O12** (average $d_{Cs3B\text{-}O}$ = 3.145 Å). **Cs4** is the other non-disordered Cs(I) counterion and adopts a coordination number of nine and interact with the cluster through **O3** and **O6** (average $d_{Cs3B\text{-}O}$ = 3.221 Å). Cs(I) cations, **Cs2** and **3**, are located in the belt area and participate in ion-pairing interactions with the UW_{10} cluster, and their proximity with the cluster, especially the U(IV) cation ($d_{U1\text{-}Cs2A\text{-}C}$ = 4.730 Å and $d_{U1\text{-}Cs3A\text{-}B}$ = 4.563 Å) may be the origin of some of the disorder in these atoms. In contrast, **Cs1** and **Cs4** are located at the periphery of the cluster and are further away from the U(IV) cations ($d_{U1\text{-}Cs1}$ = 7.155 Å and $d_{U1\text{-}Cs4}$ = 6.763 Å). The two Na(I) cations in **5** are part of a water network in the lattice, similar to **4**, and **Na1** features a typical six coordinate octahedral coordination environment. The second Na(I) counterion, **Na2**, is highly disordered, and we were not able to determine its specific coordination environment due to the disorder in the immediate vicinity of this atom. The heavier counterions in **5** again demonstrate a preference for ion-pairing interaction with the UW_{10} cluster compared to the lighter counterions which is reflected in

differences in average d_{U-M} distances which are 5.803 Å (d_{U-Cs}) and 7.646 Å (d_{U-Na}). The closest alkali metal-U(IV) interaction distances are 4.563 Å (**U1-Cs3A-B**) and 6.970 Å (**U1-Na2**), respectively, which further highlight the ability of Cs(I) to participate in stronger ion-pairing interaction with POM clusters. The observations here mirror what has already been noted for complexes **3** and **4** regarding the greater extent of association interactions with POM clusters for heavier alkali metal counterions compared to lighter counterions.

For complex **6**, the asymmetric unit contains a full UW_{10} cluster and eight Li(I) cations **Figure S8** (**Supporting Information**). All Li(I) cations in **6** exhibit typical Li(I) coordination numbers of four and notably, seven out of eight Li(I) cations in **6** also interact directly with the UW_{10} cluster. Evaluating the asymmetric unit of **6** shows that **Li1** directly interacts with the UW_{10} cluster through oxygen atoms **O4** and **O22** (average d_{Li1-O} = 2.020 Å). **Li2** is the only Li(I) cations that does not directly interact with the cluster, instead it is bound to only lattice water molecules. The remaining Li(I) cations, **Li3-8**, directly interact with the cluster through oxygen atoms **O8** (d_{Li3-O8} = 1.936 Å), **O12** ($d_{Li4-O12}$ = 1.973 Å), **O17** ($d_{Li8-O18}$ = 2.017 Å), **O23** ($d_{Li7-O23}$ = 2.028 Å), **O33** ($d_{Li6-O33}$ = 1.965 Å), and **O35** ($d_{Li5-O35}$ = 2.134 Å), respectively. The closest alkali metal cation-U(IV) interaction distance (d_{U-Li}) for **6** is 3.352 Å (**U1-Li1**) and the average d_{U-Li} is 5.766 Å. Both the d_{U-Li} and average d_{U-Li} of complex **6** are the shortest found in this study. The interactions and proximity of Li(I) cations to the UW_{10} cluster in **6** may seem inconsistent with our previous observations for complexes **1-5** where we noted an increase in stronger, ion-pairing interactions with larger alkali metal counterions. However, complex **6** is also short-lived and evolves to form complex **1** after one round of recrystallization, which is consistent with our earlier observation that the interactions between Li(I) cations and UW_{10} clusters are limited and energetically unfavorable. As such, the structural parameters for complex **6** add complexity to our findings related to UW_{10} systems and indicate that structural trends we have noted are most applicable to thermodynamically stable crystalline phases of UW_{10}.

Complexes **7** and **8** were synthesized by varying the alkali tungstate starting material rather than introducing counterions via metal chloride solutions, and these species were characterized in an identical manner to complexes **1-6** to broaden our investigation into the effects of counterion size on lattice packing. The asymmetric unit of **7** contains two halves of two unique UW_{10} moieties and eight K(I) counterions **Figures S9** and **10** (**Supporting Information**). The two unique UW_{10} (**U1** and **U2**) clusters are related to each other through a *n*-glide plane and are connected by three K(I) cations (**K1**, **K2**, and **K3**). There are ten crystallographically unique K(I) positions with some of the K(I) atoms refined with chemical occupancies of less than one due to the disorder within the lattice of **7**, and the K(I) cations in **7** adopt coordination numbers ranging from five to ten. **K1** connects both UW_{10} clusters through oxygen atoms **O9** and **O25** (average d_{K1-O} = 2.797 Å), **K2** connects both clusters through oxygen atoms **O18** and **O20** (average d_{K2-O} = 2.975 Å), and **K3** connects the clusters via oxygen atoms **O11** and **O27** (average d_{K3-O} = 2.709 Å). Potassium atoms (**K4-7**) interact with only the **U2** cluster and are located at the periphery of the POM complex. **K4** interacts through oxygen atoms **O28**, **O33**, and **O34** (average d_{K4-O} = 2.892 Å), while **K5**, **K6**, and **K7** only interact through oxygen atoms **O31** (d_{K5-O31} = 2.582 Å), **O23** (d_{K6-O23} = 2.698 Å), and **O29** (d_{K7-O29} = 2.925 Å), respectively. **K8-10** only interact with the **U1** cluster and are located in the belt region of the POM. **K8** is disordered over two positions (**K8A** and **K8B**) and interacts at both sites with the cluster via oxygen atom **O3** (average $d_{K8A/B-O3}$ = 2.796 Å). **K9** is also disordered over two dpositions (**K9A** and **K9B**) and interactions between these K(I) sites and the cluster occur through oxygen atoms **O2**, **O3**, and **O8** (average $d_{K9A/B-O2/3/8}$ = 2.796 Å). **K10** is further disordered and was satisfactorily modeled over three positions (**K10A**, **K10B**, and **K10C**), with only **K10A** interacting with the POM cluster through oxygen atom **O7** ($d_{K10A-O7}$ = 2.687 Å). The disorder exhibited by **K8-10** is similar to the disordered belt Rb(I) and Cs(I) cations in **4** and **5,** and we suspect the proximity of the cations to the cluster, and the resulting ion-pairing interactions, may be the cause of this disorder as the effects of heavy atoms in close proximity can be challenging to crystallographically resolve. The closest alkali metal-U(IV) interaction distances (d_{U-K}) for

U1 and **U2** are 4.065 Å (**U1-K9A/B**) and 5.711 Å (**U2-K3**), and the average K(I)-U(IV) interaction distance (avg $d_{U\text{-}K}$) for complex **7** is 7.190 Å. The closest and average interaction distances between K(I) and U(IV) cations in **7** are longer than those in complex **3**. Interestingly, the average $d_{U\text{-}K}$ distance in **7** is also longer compared to the average $d_{U\text{-}Na}$ distances in **2**, and while all the K(I) cations in **7** interact with the cluster, only one Na(I) cation in **2** interacts with the UW_{10} moiety. These findings illustrate that while heavier alkali metal counterions preferentially participate in ion-pairing interactions that not all interactions are equivalent in distance or their ability to effectively modulate metal-ion symmetry or crystal field splitting, which is a notable finding as it relates to tuning complexes for applications in QIS.

The asymmetric unit of **8** contains a full UW_{10} moiety and eight Cs(I) counterions, **Figure S11** (**Supporting Information**). The coordination numbers for Cs(I) cations range from six to eight, and these values are consistent with typical Cs(I) coordination environments.[49] Based on the packing of **8**, **Cs1** and **Cs2** occupy the belt area of the structure; however, unlike what is seen in complexes **4**, **5**, and **7**, these cations are not crystallographically disordered. **Cs1** interacts directly with the cluster through oxygen atom **O26** ($d_{Cs1\text{-}O26}$ = 3.171 Å), while **Cs2** interacts with the cluster through oxygen atoms **O3**, **O21**, and **O28** (average $d_{Cs2\text{-}O}$ = 3.158 Å). The rest of the Cs(I) ions in **8** are located on the periphery of the cluster where **Cs3** and **Cs5-8** interact with the cluster through oxygen atoms **O11** ($d_{Cs3\text{-}O11}$ = 3.079 Å), **O18** ($d_{Cs5\text{-}O18}$ = 2.981 Å), **O23** ($d_{Cs6\text{-}O23}$ = 3.028 Å), **O34** ($d_{Cs7\text{-}O34}$ = 3.059 Å), and **O27** ($d_{Cs8\text{-}O27}$ = 2.962 Å), respectively, while **Cs4** does not interact with the cluster. The closest Cs(I)-U(IV) distance ($d_{U\text{-}Cs}$) for this complex is 4.396 Å (**U1-Cs8**) and the average Cs(I)-U(IV) distance (avg. $d_{U\text{-}Cs}$) is 5.945 Å. Both values in complex **8** are shorter than closest and average distance values noted for Na(I) and K(I) ions in **2** and **7**, which is in agreement with findings that f-element POMs prefer ion-pairing interaction with larger counterions.

Structural Discussion

Complexes **1**-**5** are the first example of the same POM being prepared with five different counterions spanning the alkali metal series. Comparisons of the asymmetric units for **1-5** have demonstrated an evolution in POM interactions with the second coordination sphere as lighter counterions, Li(I) and Na(I), primarily form coordination networks with lattice water molecules, while heavier counterions, K(I), Rb(I), and Cs(I), prefer ion-pairing interactions that result in greater association between counterions and UW_{10} clusters. These differences are best exemplified by comparing the configuration of counterion networks within the asymmetric units of complexes **1** and **3** (**Figures S2** and **S5**, **Supporting Information**). Despite the higher number of Li(I) cations compared to Na(I) cations within the lattice in **1**, none of the Li(I) cations directly interact with the UW_{10} cluster, whereas in complex **3** all the K(I) cations directly interact with the UW_{10} moiety and only one Na(I) cation coordinates with the UW_{10} POM even though there is equal amount of Na(I) and K(I) cations within the lattice. The comparison of complex **2** with complexes **7** and **8** provides a platform for directly evaluating counterion size effects on lattice packing as these species feature a single type of alkali metal cation in the lattice and we note an increase in packing density going from **2** to **7** and **8** that highlights the increase in ion-pair interaction between the UW_{10} cluster and the heavier counterions. The decrease in unit cell volumes while keeping a constant Z value seen from **2** (6147.4(4) $Å^3$, Z = 4), **7** (5098.4(3) $Å^3$, Z=4), and **8** (2530.96(15) $Å^3$, Z = 2) captures this trend clearly as reduced volumes are associated with denser lattice packing. The volume of complex **6 (**4132.3(2) $Å^3$, Z = 4) is noteworthy as it is significantly smaller than any other complexes described herein, yet this species is a likely outlier, as highlighted above, so we have not included it as part of our structural comparisons.

In general, tetravalent UW_{10} species characterized here crystallized in monoclinic space groups, while the trivalent $LnW_{10}Na$ complexes we studied recently exclusively crystallize in the triclinic space group P-1.[15] The lesser number of counterions required to charge balance the tetravalent complexes herein is a likely cause for the differences in packing between tetravalent and trivalent complexes, although the latter systems can provide valuable information when compared to tetravalent actinide complexes as it relates to delineating size and charge effects of the metal center in the POM complexes. The ionic radius for eight

coordinate U(IV) is 1.00 Å and this is very similar to Er(III) (1.004 Å).[50] Comparing An/Ln-O bond distances in $[Er(W_5O_{18})_2]^{9-}$ (ErW_{10}) and UW_{10} reveal that d_{An-O} for UW_{10} (d_{An-O} = 2.368-2.371 Å) are slightly longer than what was noted in ErW_{10} (d_{Ln-O} = 2.3601 Å), and instead are more comparable to d_{Ln-O} values for $[Ho(W_5O_{18})_2]^{9-}$ (HoW_{10}; Ho(III) = 1.015 Å, d_{Ln-O} = 2.366 Å).[15, 50] This is an unexpected observation as metal-POM interactions with W_5 ligands are primarily expected to be ionic in bonding character. As such, one would expect the bond distances to decrease when moving from +3 to +4 metal centers of similar sizes; however, here we note that M-O bonds have been elongated. This could mean that the sandwich configuration of two W_5 ligands has a fixed cavity size which limits changes in $d_{An/Ln-O}$ distances for metal centers of similar sizes, but this explanation would not account for the elongation of the U(IV)-O distances observed herein. Another possible explanation is that the interaction between W_5 ligands and metal centers are softer in nature than anticipated, which would mean a hard-soft acid base pairing with harder tetravalent metal centers would be less preferred, thereby resulting in elongated $d_{An/Ln(IV)-O}$ distances. The average $d_{An/Ln-O}$ values for $Na_8[Th(IV)W_{10}]$ (Th(IV) = 1.05 Å, d_{An-O} = 2.423 Å) and $Na_8[Ce(IV)W_{10}]$ (Ce(IV) = 0.97 Å, d_{Ln-O} = 2.356 Å) also reveal the same elongation when compared with their respective Ln(III) size analogues, $Na_9[Gd(III)W_{10}]$ (Gd(III) = 1.053 Å, d_{Ln-O} = 2.410 Å) and $Na_9[Lu(III)W_{10}]$ (Lu(III) = 0.977 Å, d_{Ln-O} = 2.337 Å), which supports the latter hypothesis. Comparing $d_{An/Ln-O}$ distances for the different tetravalent species (Th(IV), U(IV), and Ce(IV)) reveals that M(IV)-O distances increase as the ionic radii of the M(IV) center increases with similar magnitude to what is seen in the trivalent LnW_{10} series.[15] Analysis of the crystal structures for complexes **1-8** also shows that, in general, the larger alkali metal counterions are positioned closer to the UW_{10} clusters compared to smaller metal counterions. This finding suggests the larger, softer alkali metal counterions associate more strongly with the Lindqvist POM cluster, which is in line with the hypothesis explaining the elongation of $d_{An/Ln-O}$ distances for +3 and +4 metal centers of similar sizes and consistent with the known ability of POMs to delocalize negative charges throughout entire clusters.[2, 48]

Since our overall hypothesis was that UW_{10} POMs could act as potential electron spin qubits, we investigated structural distortion parameters (DPs) for each cluster, specifically the skew angle (SA), plane angle (PA), and plane distance (PD), which can provide information about the extent of deviations from ideal D_{4d} symmetry in complexes **1-8**. In the previous section, we observed lattice packing modulations that result from changing the composition and configuration of secondary sphere elements. Based on our previous work, we anticipate that these changes in lattice packing for complexes **1-8** will also manifest in DPs for these species.[15] The details regarding the measurement of the DPs are located in the **Supporting Information** (**Figures S12** and **S13)**. Distortion parameters for complexes **1-8** are detailed in **Table 2**, and to account for the different ionic radii of the counterions as well as the variations in adopted coordination numbers, we combined the ionic radii of the counterions present within each complex and averaged these values to generate an effective ionic radii (eIR) value.[50] Details regarding the calculation of eIR and average d_{U-M} distances are located in the **Supporting Information** (**Equation S1**, **Table S3**).

Table 2. Distortion and structural parameters for complexes **1-8**.

Complexes	Skew Angle (°)	Plane Angle (°)	Plane Distance (Å)	Effective Ionic Radius (Å)	Average $d_{U-Li/K/Rb/Cs}$ (Å)	Average d_{U-Na} (Å)	Average d_{U-M} (Å)
UW_{10}Li (**1**)	0.935	2.29	0.011	0.736	6.412	6.358	6.396
UW_{10}LiF (**6**)	7.625	2.29	0.011	0.59	5.766	N/A	5.766
UW_{10}Na (**2**)	1.100	0.06	0	1.014	6.494	6.494	6.494
UW_{10}K (**3**)	2.250	2.37	0.023	1.228	6.189	6.375	6.293
UW_{10}KF (**7**)	2.238	3.67	0	1.473	7.215	N/A	7.19
UW_{10}Rb (**4**)	0.3025	2.14	0.017	1.425	6.010	8.102	6.531
UW_{10}Cs (**5**)	0.26	1.00	0.069	1.520	5.803	7.646	6.417
UW_{10} CsF (**8**)	3.343	2.41	0.027	1.736	5.941	N/A	5.941

The effective ionic radii were then plotted against the different distortion parameters, **Figure 3**. In **Figure 3a**, we observe an increase in SAs as the counterion eIR increases, except for in complexes **4**, **5**, and **6**, which are outliers in this series. **Figure 3b** reveals that there are no clear trends between the plane angle and counterion eIR values other than a qualitative increase in PA values as eIR values increase, with complexes **1** and **6** being clear outliers. **Figure 3c** also shows that there is not a clear correlation between PDs and counterion eIR values other than a general increase in PDs as eIR values increase. The PD value of complex **6** is also an outlier as it is significantly higher than the other complexes despite the small eIR of **6**. Across **Figures 3a-3c**, complex **6** displays anomalous behavior compared to other complexes within **1-8** and this may be a result of transience and instability of this species, which is not comparable with the greater stability we observed for complexes **1-5**, **7**, and **8**. The average distance between U(IV) cations and alkali metal counterions is another variable that was also investigated and compared with structural DPs for complexes **1-8**. The average U(IV)-counterion distances (average $d_{U\text{-}M}$; M = Li(I), Na(I), K(I), Rb(I), Cs(I)) are plotted against the DPs in **Figure 4**. **Figure 4a** reveals that SAs decrease as the average $d_{U\text{-}M}$ distance increases, except for complex **7**. There is also a general decrease in PAs as the average $d_{U\text{-}M}$ distance decreases **(Figure 4b**), consistent with the trend we noted for SAs, with complex **7** again being a clear outlier in this comparison. The comparison of PDs with average $d_{U\text{-}M}$ distance reveals that plane distances in **1-8** decrease as the average $d_{U\text{-}M}$ distance increase, mimicing the observations from SA and PA comparisons, with complex **5**the the outlier in this plot. Worthy of an additional comment, it is notable that **6** display unusually high degrees of distortion as observed in SA and PD values that are almost twice as large as distortion parameter values we obtained for other complexes. This further suggests that complex **6** is an unstable species, which may be a result of weak interactions between Li(I) cations and the UW_{10} cluster that allow for greater deviations from ideal symmetry for this complex.

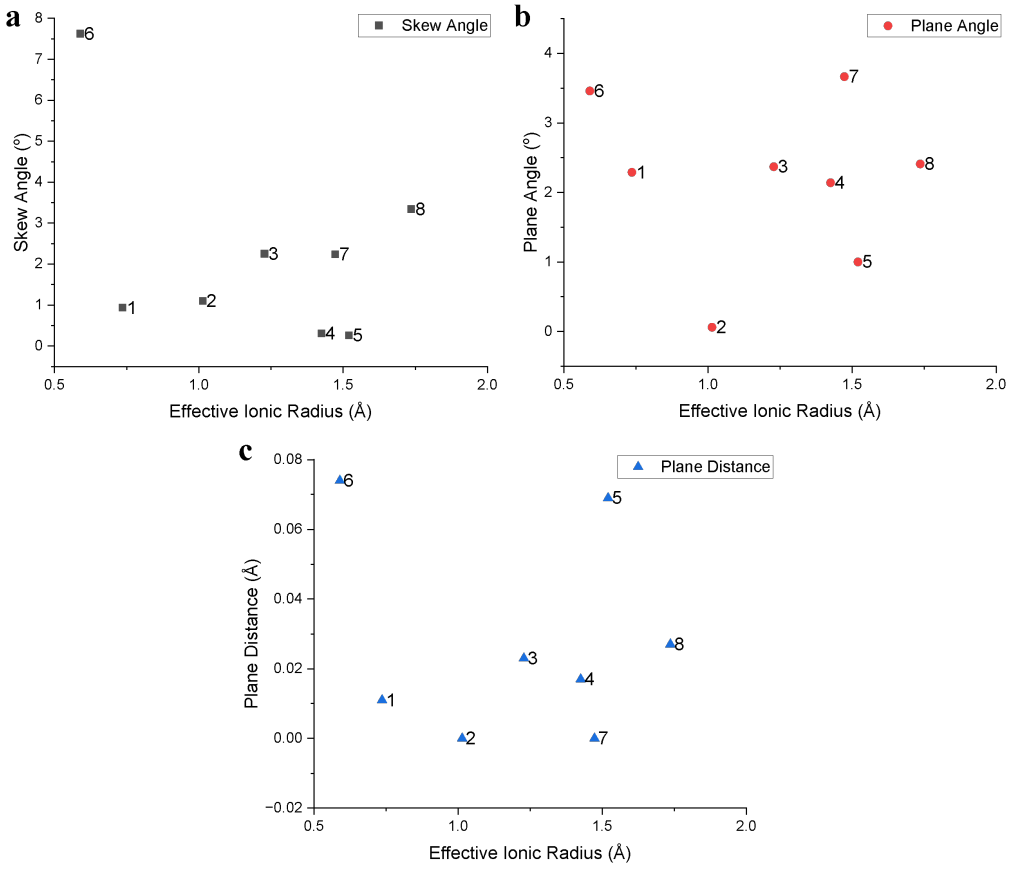

Figure 3. Plots of skew angle (SA) v. counterion effective ionic radii (eIR) (**a**), plane angle (PA) v. eIR (**b**), and plane distance (PD) v. eIR (**c**) for complexes **1**-**8**.

To more rigorously understand how counterions affect complex DPs, partial least squares analysis (PLS) was conducted, **Figures S14-S19** (**Supporting Information**). Counterion eIR and average d_{U-M} distance were chosen as independent variables to capture how changes in counterion size and interaction distances with POM clusters impacted DPs and unit cell parameters and average d_{U-O} distances were chosen as independent variables to capture how changes in overall lattice packing impacted DPs. The full details regarding the PLS analysis can be found in the **Partial Least Square Analysis** section of the **Supporting Information**. Initially, the PLS regression models were unable to model the observed DP variances while passing cross-validation tests that prevent model overfitting, **Figure S14** (**Supporting Information**). When values involving complex **6** were removed from the analysis, cross-validated models could be built for SA and PD values and the independent variables described above. According to PLS analysis, four factors can be synthesized out of the independent variables to account for 87.9% of the variance seen in skew angle values, **Figure S15** (**Supporting Information**) and based on the loading scores we were able to narrow the cause of SA variance to unit cell volume and counterion eIR values (**Figures S15** and **S16**, **Supporting Information**). As the latter affects the packing, and thus the unit cell volume, it is highly probable that counterion eIR has the largest impact on SA values. The PLS model where plane distance is the dependent variable produces one latent variable that accounts for 69.1% of the variance observed in these DP values, **Figure S18** and **S19** (**Supporting Information**). Loading scores show that the β angle and average d_{U-M} distance are the two most correlated variables with complex PDs, and consistent with our analysis above, we attribute changes in average d_{U-M} distances to be the primary driver in plane distance variance. Despite the lack of statistical correlation found between PA values and the independent variables, **Figure S17** (**Supporting Information**), PLS analysis still found that structural parameters, especially the counterion eIR and the average d_{U-M} distance, were highly correlated with PA values, which supports our approach for modifying the effective symmetry around the metal center by tuning the composition and packing of lattice counterions.

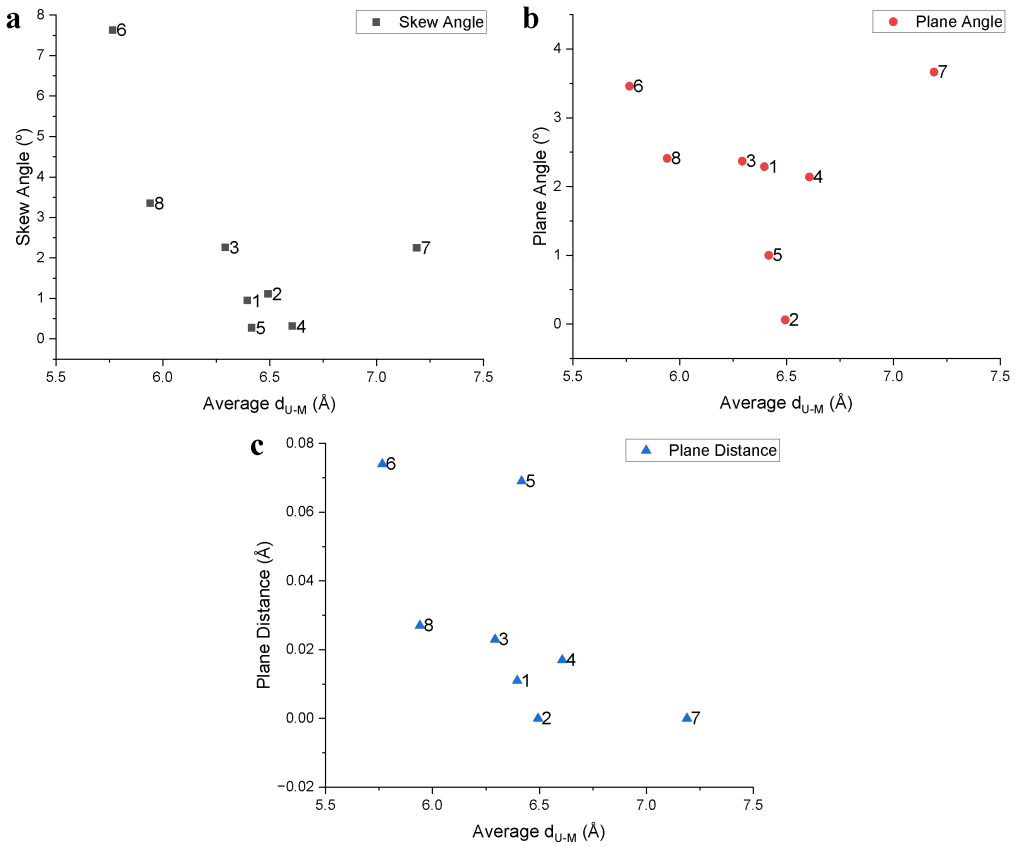

Figure 4. Plots of SA v. average d_{U-M} distance (**a**), PA v. avg. d_{U-M} distance (**b**), and PD v. avg. d_{U-M} distance (**c**) for complexes **1**-**8**.

Vibrational Spectroscopy

The FIR and Raman spectra of complexes **1-8** were collected on single crystals and features were identified through peak fitting regimes executed using the Origin2024 software package. This section will be split into two different parts with the initial discussion focused on the FIR spectra and the second part describing results from Raman spectra. Raw data, background subtracted spectra, and fit parameters for the FIR and Raman spectra of complexes **1-8** can be found in **Figures S20-S37** (**Supporting Information**), and the data here are the first examples of vibrational spectroscopy measurements conducted on UW_{10} POMs. Despite the similarities between the first coordination spheres of UW_{10} POMs, FIR and Raman spectra exhibit distinct changes in vibrational features that we attribute to differences in interactions between POM clusters and alkali metal counterions, **Figures 5** and **6**. FIR vibrational assignments were made using peaks that had been previously identified in the literature, and were primarily based on our recent work and a 2021 study from Blockmon *et al*.[15, 51]

Since the FIR spectra of complex **2**, $Na_8[UW_{10}]$, is akin to the FIR spectra of HoW_{10}, it was chosen to be our model species for vibrational modes assignments, which were then translated to complexes **1** and **3-8**. Based on the peak fitting regime, complex **2** possesses six features in the FIR (**Figure S23**, **Supporting Information**), similar to what was observed for HoW_{10}. The peak centered at 363 cm^{-1} matches well with the $\delta/\rho(HoO_4)$ mode and was assigned here as the $\delta/\rho(UO_4)$ mode. The peak at 322 cm^{-1} is consistent with the frequency of the $\nu/\rho(HoO_8)$ mode; thus, we assigned it here as the $\nu/\rho(UO_8)$ mode. The peak centered at 191 cm^{-1} is in agreement with where we observed the $\rho(HoO_8)$ mode, and here it was assigned as the $\rho(UO_8)$ mode. Finally, the peak centered at 145 cm^{-1} was assigned as a $\nu(WO_5)_2$ mode, which is also consistent with results from our group and Blockmon and colleagues.[15, 51] The peaks at 169 cm^{-1} and 129 cm^{-1} do not match with any known FIR stretches in the literature for U(IV), and thus were not assigned. The complete list of FIR vibrational mode assignments for complexes **1-8** can be found in **Table 3**.

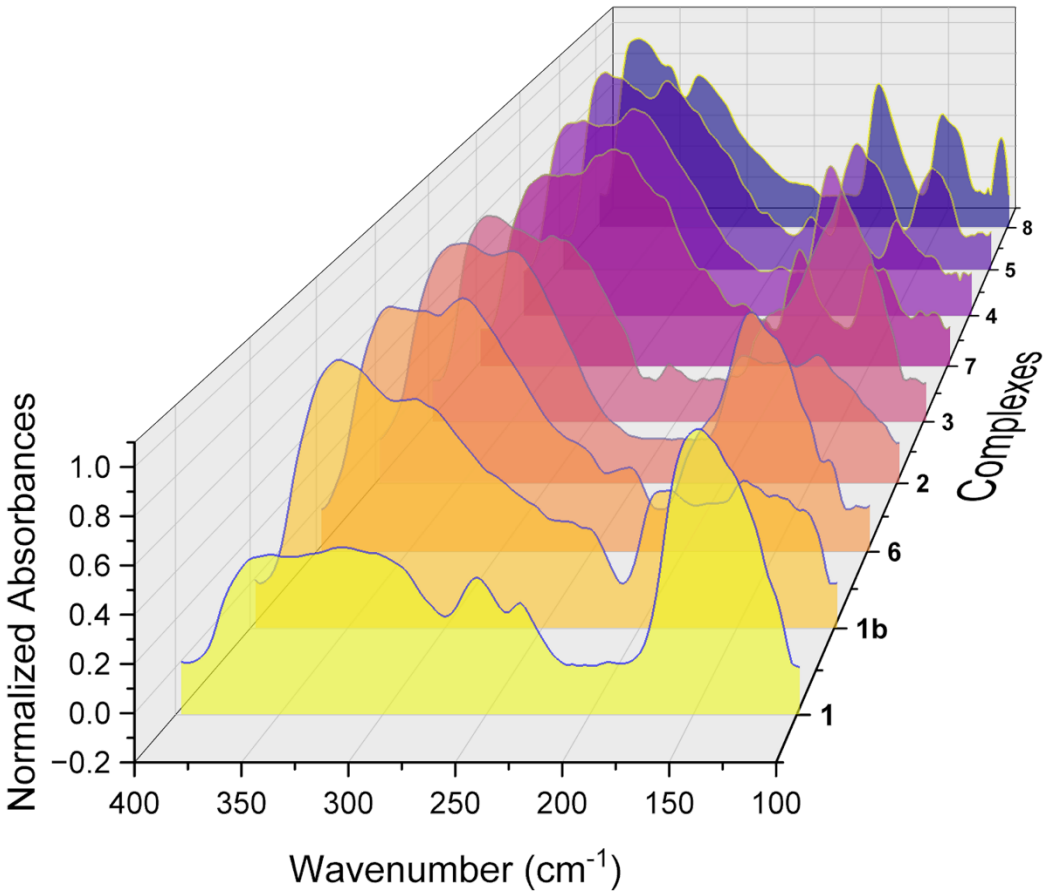

Figure 5. Normalized and background subtracted far-IR spectra for complexes **1-8**.

Comparing the FIR spectra across complexes **1-8**, the spectrum of **2** is qualitatively similar to the spectra for **1, 3**, and **6**, while complexes **4**, **5, 7**, and **8** feature spectra that are different than complex **2**, yet similar to each other. The FIR spectrum for complex **1**, $Li_5Na_3[UW_{10}]$, exhibits nine features, **Figure S20** (**Supporting Information**) compared to the six observed for **2**. The peak centered at 361 cm^{-1} was assigned as a $\delta/\rho(UO_4)$ mode, while the peaks at 330 cm^{-1} and 142 cm^{-1} were assigned to $\nu/\rho(UO_8)$ and $\nu(WO_5)_2$ modes, respectively. There is no peak that can be associated with the $\rho(UO_8)$ mode in **1**. The additional peaks centered at 373 cm^{-1}, 292 cm^{-1}, 254 cm^{-1}, 232 cm^{-1}, 158 cm^{-1} and 120 cm^{-1} do not match with any known FIR stretches in the literature for U(IV) and thus were not assigned. The bands observed at 254 cm^{-1} and 232 cm^{-1} may originate due to LiCl contamination in the sample; however, this is unlikely as the

collections are conducted on single crystals and done in triplicate. The FIR spectrum for polymorph complex **1b** was also collected and features twelve peaks, **Figure S21** (**Supporting Information**). The peak centered at 354 cm^{-1} was assigned as a $\delta/\rho(UO_4)$ mode, while the peaks centered at 314 cm^{-1}, 195 cm^{-1}, and 146 cm^{-1} were assigned to the $\nu/\rho(UO_8)$, $\rho(UO_8)$, and $\nu(WO_5)_2$ modes, respectively. The spectrum for **1b** also includes the peaks seen in **1** at 259 cm^{-1} and 232 cm^{-1} as well as the two unassigned peaks at 166 cm^{-1} and 125 cm^{-1}; however, the FIR spectrum for **1b** also features extra peaks centered at 221 cm^{-1}, 184 cm^{-1}, and 111 cm^{-1}. As these peaks do not match with known FIR peak assignments, and computational calculations are outside our abilities and the scope of this study, the extra peaks for **1b** were not assigned. The FIR spectrum for complex **6**, $Li_8[UW_{10}]$, includes eleven peaks that are centered at frequencies that are very similar to those observed for complex **1**, **Figure S22** (**Supporting Information**). The peaks at 351 cm^{-1}, 322 cm^{-1}, 192 cm^{-1}, and 142 cm^{-1} were assigned to the $\delta/\rho(UO_4)$, $\nu/\rho(UO_8)$, $\rho(UO_8)$ and $\nu(WO_5)_2$ modes, respectively, while the remainder of the peaks centered at 294 cm^{-1}, 254 cm^{-1}, 229 cm^{-1}, 164 cm^{-1}, 130 cm^{-1}, and 120 cm^{-1} do not match with known FIR peak assignments for W_{10} POM systems and were not assigned. Overall, the FIR spectra of **1**, **1b**, and **6** display similar features with the notable exception of the absence of the $\rho(UO_8)$ stretch in the spectrum of **1**. Finally, the FIR spectrum for complex **3** exhibits nine features similar to **1**, **Figure S24** (**Supporting Information**) and the peaks centered at 358 cm^{-1} and 323 cm^{-1} were assigned as $\delta/\rho(UO_4)$ and $\nu/\rho(UO_8)$ modes, while the peaks centered at 194 cm^{-1} and 145 cm^{-1} were assigned as $\rho(UO_8)$ and $\nu(WO_5)_2$ modes. The remaining peaks centered at 374 cm^{-1}, 292 cm^{-1}, 252 cm^{-1}, 166 cm^{-1}, and 127 cm^{-1} do not match with any known FIR stretches in the literature for U(IV) and thus were not assigned.

Table 3. Far-IR (FIR) mode assignments for complexes **1-8**.

Complex	$\delta/\rho(UO_4)$ modes (cm^{-1})	$\nu/\rho(UO_8)$ modes (cm^{-1})	$\rho(UO_8)$ modes (cm^{-1})	$\nu(WO_5)_2$ modes (cm^{-1})	Unassigned (cm^{-1})
UW10 Li (**1**)	360.77	329.75	-	142.32	119.93, 158.27, 232.46, 253.90, 291.80, 373.34
UW10 Li 2 (**1b**)	353.83	314.41	195.11	146.06	110.79, 124.70, 165.85, 221.36, 232.43, 259.25, 370.82
UW10 LiF (**6**)	350.91	321.70	192.10	142.43	119.70, 130.10, 163.88, 229.09, 253.65, 293.85
UW10 Na (**2**)	363.21	321.98	191.14	145.02	128.99, 168.99
UW10 K (**3**)	358.22	322.50	194.41	145.24	127.24, 165.74, 251.96, 291.73, 374.52
UW10 KF (**7**)	369.71, 356.03	312.47	194.74	151.25	110.67, 118.09, 142.21,180.85, 215.56, 227.72, 250.63, 266.81, 277.63, 378.79
UW10 Rb (**4**)	361.33	329.30	194.37	148.90	124.05, 136.54, 181.45, 280.69, 297.05, 375.85
UW10 Cs (**5**)	360.15	325.75	195.29	144.34	131.83, 178.66, 223.84, 250.90, 286.42, 375.90
UW10 CsF (**8**)	363.38	325.63	195.29	149.30	104.68, 137.50, 184.56, 246.39, 299.95, 345.86, 378.04

The FIR spectrum for complex **4**, $Rb_6Na_2[UW_{10}]$, includes ten peaks with those centered at 376 cm^{-1} and 361 cm^{-1} assigned as $\delta/\rho(UO_4)$ modes and the peaks centered at 329 cm^{-1}, 194 cm^{-1}, and 149 cm^{-1} assigned as $\nu/\rho(UO_8)$, $\rho(UO_8)$, and $\nu(WO_5)_2$ modes, respectively, **Figure S26** (**Supporting Information**). The remaining features at 291 cm^{-1}, 281 cm^{-1}, 181 cm^{-1}, 136 cm^{-1}, and 124 cm^{-1} do not match with known FIR peak assignments and were not assigned. The difference in spectral features between complexes **4**-**8** and complexes **1**-**3** can be most clearly observed in the lower wavenumber region of the FIR (250-100 cm^{-1}). The peak centered around 165 cm^{-1} in the spectra for complexes **1**-**3** and **6** is absent for complexes **4**-**8** (excluding **6**), and instead lower energy features are split into a series of smaller peaks. The FIR spectrum for complex **5**, $Cs_{5.5}Na_{2.5}[UW_{10}]$, also includes ten features that were similarly assigned to **4**, **Figure S27** (**Supporting Information**). Peaks centered at 360 cm^{-1} and 326 cm^{-1} were assigned as $\delta/\rho(UO_4)$ and $\nu/\rho(UO_8)$ modes, respectively, while the peaks centered at 195 cm^{-1} and 144 cm^{-1} were assigned as $\rho(UO_8)$ and $\nu(WO_5)_2$ modes. The remaining peaks centered at 286 cm^{-1}, 251 cm^{-1}, 224 cm^{-1}, 179 cm^{-1}, and 134 cm^{-1} do not match with known FIR peak assignments for W_{10} POM systems and were not assigned as a result. The FIR spectrum for complex **7**, $K_8[UW_{10}]$, includes the most features (**Figure S25**, **Supporting Information**) we observed in this family of complexes with fifteen peaks noted between 400-100 cm^{-1}. The peaks centered at 370 cm^{-1} and 356 cm^{-1} were assigned as $\delta/\rho(UO_4)$ modes, while the peaks centered at 312 cm^{-1}, 195 cm^{-1}, and 151 cm^{-1} were assigned as $\nu/\rho(UO_8)$, $\rho(UO_8)$, and $\nu(WO_5)_2$ modes, respectively. The remaining peaks that were unassigned as they do not match any known FIR assignments for U(IV) complexes and are located at 278 cm^{-1}, 267 cm^{-1}, 251 cm^{-1}, 228 cm^{-1}, 216 cm^{-1}, 181 cm^{-1}, 142 cm^{-1}, 118 cm^{-1}, and 111 cm^{-1}. The abundance of features in the FIR spectrum of **7** can be explained by its distinct crystal structure as **7** is the only species with two unique UW_{10} moieties within its unit cell, which means that it is possible to observe the same mode for each moiety with peak splitting due to the difference in local environments. The FIR spectrum for complex **8**, $Cs_8[UW_{10}]$, includes eleven features that are very similar to those included in the FIR spectrum for **5** (**Figure S28**, **Supporting Information**). The peaks centered at 363 cm^{-1}, 326 cm^{-1}, 196 cm^{-1}, and 149 cm^{-1} are assigned as $\delta/\rho(UO_4)$, $\nu/\rho(UO_8)$, $\rho(UO_8)$, and $\nu(WO_5)_2$ modes, respectively, while the stretches centered at 346 cm^{-1}, 300 cm^{-1}, 246 cm^{-1}, 185 cm^{-1}, 137 cm^{-1}, and 107 cm^{-1} do not match with known vibrational frequencies for W_{10} POMs so these peaks remain unassigned.

For the Raman spectra of **1**-**8**, we once again utilized vibrational assignments from the literature, mainly from the works of Kazanskii and colleagues and Shiozaki *et al.*,[45, 47] to aid in making peak fitting assignments. Similar to our treatment of FIR results, we used complex **2**, $Na_8[UW_{10}]$, as our model species for vibrational modes assignments, and the Raman spectrum for **2** exhibits fifteen features over the spectral range 1050-100 cm^{-1}, **Figure S32** (**Supporting Information**). The peaks centered at 969 cm^{-1}, 949 cm^{-1}, and 937 cm^{-1} were assigned as ν(W=O) modes. The peak centered at 880 cm^{-1} is assigned as a ν(U-O-W) mode, while the peaks centered at 835 cm^{-1}, 814 cm^{-1}, 581 cm^{-1}, and 550 cm^{-1} were assigned as ν(W-O-W) modes. The bands centered at 434 cm^{-1} and 361 cm^{-1} were assigned as δ(W-O-W / W=O / U-O-W) modes and the remaining features centered at 232 cm^{-1}, 212 cm^{-1}, 179 cm^{-1}, 164 cm^{-1}, and 142 cm^{-1} were assigned as POM deformation modes. The full vibrational mode assignments for the Raman spectra of **1**-**8** can be found in **Table 4**.

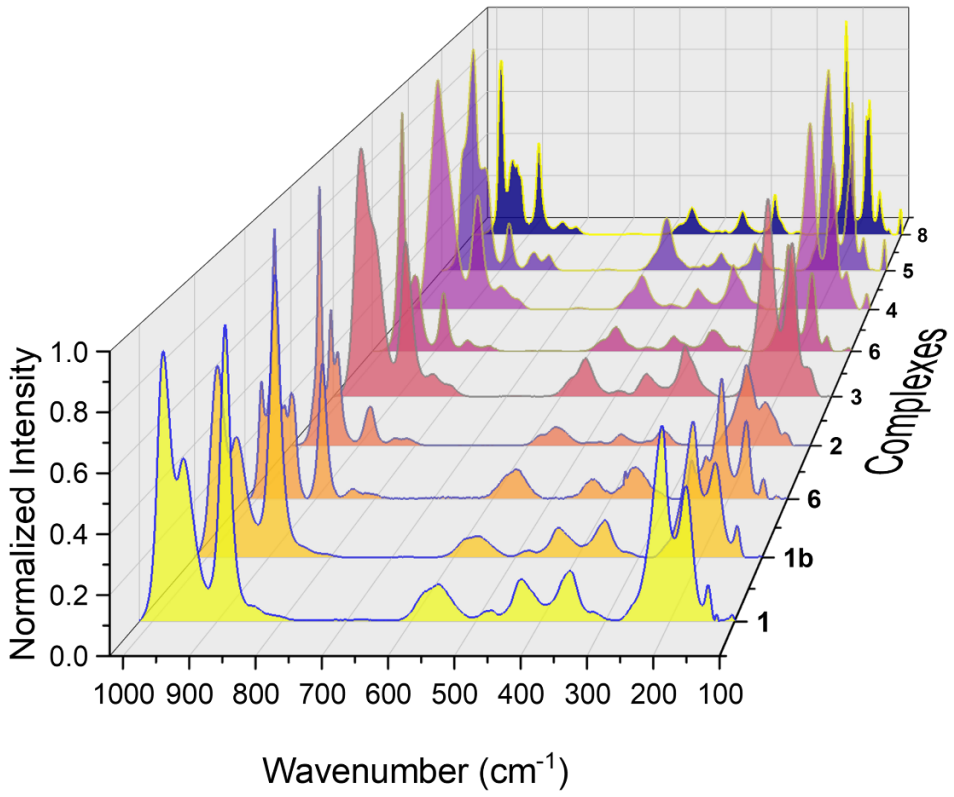

Figure 6. Normalized and background subtracted Raman spectra for complexes **1**-**8**.

The Raman spectra for complexes **1** and **3**-**8** (**Figures S29**-**S31** and **S33**-**S37**, **Supporting Information**) display different numbers of peaks compared to the spectrum for **2**; however, the major features are in identical regions, **Figure 6**. The Raman spectrum of **1**, $Li_5Na_3[UW_{10}]$, includes five fewer peaks than **2**, **Figure S29** (**Supporting Information**). The peaks centered at 982 and 951 cm^{-1} were assigned as ν(W=O) modes, while peaks centered at 887 cm^{-1} and 563 cm^{-1} were assigned as ν(U-O-W) and ν(W-O-W) modes, respectively. Peaks centered at 480 cm^{-1}, 426 cm^{-1}, and 357 cm^{-1} were assigned as δ(W-O-W/W=O/U-O-W) modes and the remaining peaks centered at 214 cm^{-1}, 175 cm^{-1}, and 140 cm^{-1} were assigned as POM deformation modes. Complex **1b** has an almost identical Raman spectrum to **1** with one notable difference at 585 cm^{-1} that we assign as an extra ν(W-O-W) stretch, **Figures S29** and **S30** (**Supporting Information**). The similarity between the Raman spectra of the two polymorph is surprising due to the differences in crystallographic unit cells, **Tables 1** and **S1** (**Supporting Information**) and the distinctions between the FIR spectra of **1** and **1b**, **Figures S20** and **S21** (**Supporting Information**). The source of this similarity could be decomposition of the less stable **1** to the more favorable **1b** due to dehydration of the lattice when the crystals are taken out of the mother liquor during the Raman data collection process. This dehydration happens in a matter of minutes for **1**-**8** and has been observed in our previous work focused on LnW_{10} complexes and in the literature as well.[15, 51]

Table 4. Raman mode assignments for complexes **1**-**8**.

Complexes	ν(W=O) modes (cm^{-1})	ν(U-O-W) modes (cm^{-1})	ν(W-O-W) modes (cm^{-1})	δ(W-O-W / W=O / U-O-W) modes (cm^{-1})	POM deformation modes (cm^{-1})
UW10 Li (**1**)	950.55, 982.33	886.97	562.53	356.81, 426.40, 480.03	140.23, 174.52, 214.35
UW10 Li 2 (**1b**)	950.57, 982.72	889.20	565.58, 584.91	356.72, 427.06, 480.33	140.06, 175.25, 214.04
UW10 LiF (**6**)	938.95, 952.30, 969.97, 991.32	887.97	560.50, 584.52, 800.99, 834.25	347.37, 365.47, 430.69	140.10, 170.23, 211.76, 238.62
UW10 Na (**2**)	936.59, 949.22, 969.45	879.97	549.25, 581.24, 814.05, 835.55	360.88, 433.75	142.36, 163.62, 178.57, 211.75, 232.24
UW10 K (**3**)	944.52, 969.32	884.56	552.18, 562.71, 799.95, 835.49	367.06, 440.48	139.17, 172.90, 218.75
UW10 KF (**7**)	935.91, 962.94	882.16	552.41, 585.25, 795.28, 835.20	359.72, 371.35, 417.20, 439.73	145.54, 175.01, 219.94
UW10 Rb (**4**)	941.14, 963.22	880.81	551.19, 562.35, 803.48, 833.64	351.49, 371.32, 440.02, 492.70	104.42,142.96, 172.06, 218.93, 323.62
UW10 Cs (**5**)	927.46, 955.67, 976.41	879.44	554.51, 799.82, 830.47	363.15, 372.30, 442.49	102.92, 145.29, 170.28, 217.13, 228.46
UW10 CsF (**8**)	920.64, 934.92, 959.44	877.97	548.29, 580.46, 796.36, 826.15	363.33, 371.44, 440.61	101.68, 145.97, 167.58, 175.10, 217.52, 241.54

The Raman spectrum of **3**, $K_4Na_4[UW_{10}]$, includes one less ν(W=O) mode and two less features in the POM deformation region compared to **2**, and twelve peaks overall, **Figure S33** (**Supporting Information**). The peaks centered at 969 cm^{-1} and 945 cm^{-1} were assigned as ν(W=O) modes. The peak centered at 885 cm^{-1} was assigned as a ν(U-O-W) mode, while the peaks centered at 835 cm^{-1}, 800 cm^{-1}, 563 cm^{-1}, and 552 cm^{-1} were assigned as ν(W-O-W) modes. Peaks centered at 440 cm^{-1} and 367 cm^{-1} were assigned as δ(W-O-W/W=O/U-O-W) modes and the remaining peaks centered at 219 cm^{-1}, 173 cm^{-1}, and 139 cm^{-1} were assigned as POM deformation modes. The Raman spectrum of **4**, $Rb_6Na_2[UW_{10}]$, exhibits one less feature in the ν(W=O) region and two more features in the δ(W-O-W / W=O / U-O-W) region compared to **2**, and includes sixteen total peaks **Figure S35** (**Supporting Information**). The stretches centered at 963 cm^{-1} and 941 cm^{-1} were assigned as ν(W=O) modes and the peak centered at 881 cm^{-1} was assigned as a ν(U-O-W) mode. Stretches centered at 834 cm^{-1}, 803 cm^{-1}, 562 cm^{-1}, and 551 cm^{-1} were assigned as ν(W-O-W) modes, while the peaks centered at 440 cm^{-1}, 417 cm^{-1}, 371 cm^{-1}, and 351 cm^{-1} were assigned as δ(W-O-W/W=O/U-O-W) modes. The remaining peaks centered at 324 cm^{-1}, 219 cm^{-1}, 172 cm^{-1}, 143 cm^{-1}, and 104 cm^{-1}were assigned as POM deformation modes. The Raman spectrum of **5**, $Cs_{5.5}Na_{2.5}[UW_{10}]$, includes one less feature in the ν(W-O-W) region and one more feature in the δ(W-O-W / W=O / U-O-W) region compared to **2**, and both spectra feature fifteen peaks, **Figures S32** and **S36** (**Supporting Information**). The stretches centered at 976 cm^{-1}, 956 cm^{-1}, and 927 cm^{-1} were assigned as ν(W=O) modes and the peak centered at 879 cm^{-1} was assigned as a ν(U-O-W) mode. The peaks centered at 830 cm^{-1}, 800 cm^{-1}, and 555 cm^{-1} were assigned as ν(W-O-W) modes, while the peaks centered at 442 cm^{-1}, 372 cm^{-1}, and 363 cm^{-1} were assigned

as δ(W-O-W/W=O/U-O-W) modes. The remaining peaks centered at 228 cm^{-1}, 217 cm^{-1}, 170 cm^{-1}, 145 cm^{-1}, and 103 cm^{-1} were assigned as POM deformation modes.

The Raman spectrum for **6**, $Li_8[UW_{10}]$, displays one additional feature in both the ν(W=O) and δ(W-O-W/ W=O/ U-O-W) regions and one less stretch in the POM deformation mode region compared to **2**, and sixteen peaks overall, **Figure S31** (**Supporting Information**). The bands centered at 991 cm^{-1}, 970 cm^{-1}, 952 cm^{-1}, and 939 cm^{-1} were assigned as ν(W=O) modes and the peak centered at 888 cm^{-1} was assigned as a ν(U-O-W) mode. The peaks centered at 834 cm^{-1}, 801 cm^{-1}, 584 cm^{-1}, and 561 cm^{-1} were assigned as ν(W-O-W) modes, while the stretches centered at 431 cm^{-1}, 365 cm^{-1}, and 347 cm^{-1} were assigned as δ(W-O-W / W=O / U-O-W) modes. The remaining peaks centered at 239 cm^{-1}, 212 cm^{-1}, 170 cm^{-1}, and 140 cm^{-1} were assigned as POM deformation modes. The Raman spectrum of **7**, $K_8[UW_{10}]$, includes one less feature in the ν(W=O) region, one more feature in the δ(W-O-W / W=O / U-O-W) region, and two less features in the POM deformation region compared to **2**, and contains fourteen assignable peaks, **Figure S34** (**Supporting Information**). The peaks centered at 963 cm^{-1} and 936 cm^{-1} were assigned as ν(W=O) modes and the peak centered at 882 cm^{-1} was assigned as a ν(U-O-W) mode. The stretches centered at 835 cm^{-1}, 795 cm^{-1}, 585 cm^{-1}, and 552 cm^{-1} were assigned as ν(W-O-W) modes, while the peaks centered at 440 cm^{-1}, 417 cm^{-1}, 371 cm^{-1}, and 360 cm^{-1} were assigned as δ(W-O-W/W=O/U-O-W) modes. The remaining peaks centered at 220 cm^{-1}, 175 cm^{-1}, and 146 cm^{-1} were assigned as POM deformation modes. Finally, the Raman spectrum for **8**, $Cs_8[UW_{10}]$, exhibits one more feature in both the δ(W-O-W / W=O / U-O-W) and POM deformation regions compared to **2**, and includes seventeen peaks overall, **Figure S37** (**Supporting Information**). The peaks centered at 959 cm^{-1}, 935 cm^{-1}, and 921 cm^{-1} were assigned as ν(W=O) modes and the peak centered at 878 cm^{-1} was assigned as a ν(U-O-W) mode. The stretches centered at 826 cm^{-1} 796 cm^{-1}, 580 cm^{-1}, and 548 cm^{-1} were assigned as ν(W-O-W) modes and the peaks centered at 441 cm^{-1}, 371 cm^{-1} and 363 cm^{-1} were assigned as δ(W-O-W/W=O/U-O-W) modes. The remaining peaks centered at 242 cm^{-1}, 218 cm^{-1}, 175 cm^{-1}, 168 cm^{-1}, 146cm^{-1}, and 102 cm^{-1} were assigned as POM deformation modes.

In general, the Raman spectra of **1**-**8** are more alike compared to FIR spectra for the same species; however, the differences in number of peaks suggests there is a distinct vibrational energy splitting regime for each of the complexes that may be related to the composition and packing of the lattice. When we directly compare related species, such as **1**, **1b**, and **6**, we note that the spectra of **1** and **1b** are nearly identical, whereas the spectrum for **6** includes extra features located in the ν(W=O) and ν(W-O-W) regions. These differences may be a result of structural changes for **6**, which features extensive interactions between the Li(I) cations and the UW_{10} cluster, in contrast to **1**, that could split the degeneracy of the ν(W=O) and ν(W-O-W) modes in these complexes, especially for the ν(W=O) mode as there are abundant interactions between the terminal cluster oxygen atoms and the Li(I) counterions in **6**. However, if this was the case we would expect to see more extensive peak splitting in the Raman spectra of **3**-**8** (excluding **6**), rather than the more limited selection of ν(W=O) stretches we observed (**Figures S33**-**37**, **Supporting Information**). An alternate explanation is that the ion-pairing interactions observed for larger counterions in **3**-**8** (excluding **6**) can shift the frequency of ν(W=O) peak, while the unique interactions provided by the Li(I) cations in **6** lead to changes in packing symmetry that split the degeneracy of the ν(W=O) band. **Figure S38** (**Supporting Information**) shows a comparison of ν(W=O) frequencies versus counterion eIR values wherein a redshift in the ν(W=O) frequency as the eIR increases is noted. This trend confirms that the ν(W=O) band frequency shifts as a function of counterion size and suggest interactions between the cluster and the larger counterions may reduce the strength of the ν(W=O) bond. To further elucidate the origins of vibrational band splitting, computational effort is required that is outside the scope of this investigation; however, we can confirm that there are overall shifts in the major Raman and FIR features as a function of structural parameters that will be further explored in the next section.

Structural-Vibrational Correlations

We used qualitative comparisons and partial least square (PLS) analysis to understand the specific correlations between structural and vibrational features in UW_{10} systems. The structural features evaluated in this study include skew angles (SA), plane angles (PA), plane distances (PD), effective ionic radii (eIR), and average $d_{U\text{-}M}$ distances, which capture structural characteristics within the first and second coordination spheres. All relevant structural parameters are tabulated in **Table 2**. The vibrational bands of interest here are the $\nu(WO_5)_2$, $\rho(UO_8)$, $\nu/\rho(UO_8)$, and $\delta/\rho(UO_4)$ modes from the FIR and the δ(W-O-W / W=O / U-O-W), ν(W-O-W), ν(U-O-W), and low energy POM deformation modes from the Raman. We will first discuss the correlations found between structural parameters and FIR modes before moving onto analysis featuring Raman modes.

The qualitative comparison of DPs versus the $\nu(WO_5)_2$ mode reveals a general redshift of the $\nu(WO_5)_2$ frequencies as the SAs and PDs increase in value, **Figure S39** (**Supporting Information**). In contrast, the plane angles do not display any clear correlation with the $\nu(WO_5)_2$ frequencies, **Figure S39** (**Supporting Information**). When the frequencies of $\nu(WO_5)_2$ FIR modes are compared to counterion eIR values and average $d_{U\text{-}M}$ distances we note linear increases as both structural parameters increase, **Figures 7** and **S39** (**Supporting Information**). There were a couple of outliers in the comparison between $\nu(WO_5)_2$ frequencies and average $d_{U\text{-}M}$ distance with complexes **5** and **8** not following the linear trend. PLS analysis on this FIR mode produces two latent variables that account for 89.1% of variance observed in the $\nu(WO_5)_2$ frequencies, **Figure S40** and **41** (**Supporting Information**). Based on the X- and Y-loading plots, **Figure S40** (**Supporting Information**), counterion eIR and average $d_{U\text{-}M}$ are the two most correlated variables with the $\nu(WO_5)_2$ frequencies, and this quantitative conclusion matches the qualitative observations highlighted earlier.

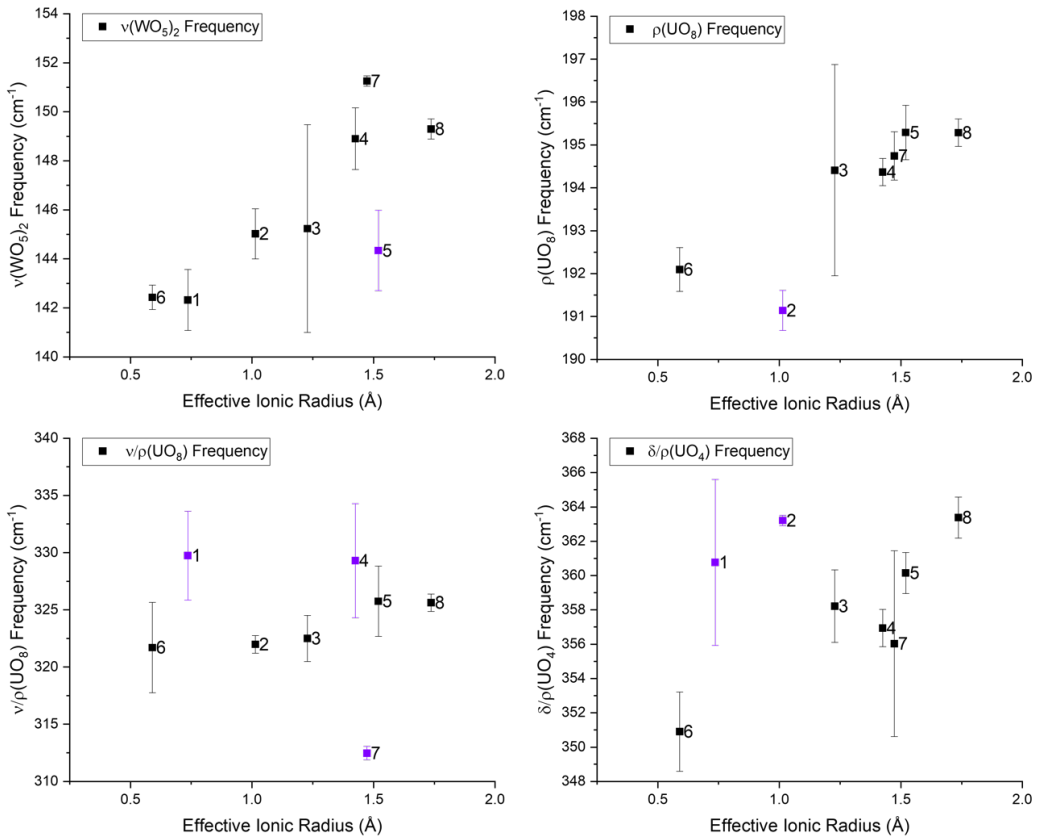

Figure 7. (**Top Left**) Plot of FIR $\nu(WO_5)_2$ frequencies vs. counterion eIR values, (**Top Right**) Plot of FIR $\rho(UO_8)$ frequencies vs. counterion eIR values, (**Bottom Left**) Plot of FIR $\nu/\rho(UO_8)$ frequencies vs. counterion eIR values, and (**Bottom Right**) Plot of FIR $\delta/\rho(UO_4)$ frequencies vs. counterion eIR values. Purple data points indicate outliers to observed trends.

Qualitative comparisons of FIR $\rho(UO_8)$ mode frequencies and structural parameters were also conducted, except for complex **1** where this vibrational stretch was not observed in the corresponding FIR spectrum (**Figures 7 and S42** (**Supporting Information**).The comparisons of $\rho(UO_8)$ mode frequencies versus structural distortion parameters reveal general redshifts in the $\rho(UO_8)$ frequencies as DP values increase with the skew angle comparison displaying the most linear correlation, **Figure S42** (**Supporting Information**). In contrast, the plot of $\rho(UO_8)$ frequencies versus counterion eIR shows a linear correlation between this FIR mode frequency and the eIR value with complex **2** being an outlier to this trend, **Figure 7**. Similarly, when we compare $\rho(UO_8)$ frequencies versus average $d_{U\text{-}M}$ distance we also observe a blueshift in vibrational frequencies as the average $d_{U\text{-}M}$ distance increases, **Figure S42** (**Supporting Information**). PLS regression analysis (**Figures S43** and **S44**, **Supporting Information**) extracted three latent variables out of the independent variables which managed to account for 96.1% of the variance observed in $\rho(UO_8)$ frequencies. This result is consistent with our qualitative analysis, and according to the X- and Y-loading plots, **Figure S43** (**Supporting Information**), the variables with the strongest correlation with the $\rho(UO_8)$ frequencies are counterion eIR followed by the average $d_{U\text{-}M}$ distance.

Comparing $\nu/\rho(UO_8)$ mode frequencies with skew angle and plane angle values reveals redshifts in this stretch as both DP values increase, **Figure S45** (**Supporting Information**). In contrast, the plot of $\nu/\rho(UO_8)$ frequencies versus plane distance values do not show any correlation, **Figure S45** (**Supporting Information**). When $\nu/\rho(UO_8)$ mode frequencies are compared with counterion eIR a blue shift in vibrational frequencies is noted as eIR values increase, **Figure 7**, which is echoed by the plot of $\nu/\rho(UO_8)$ frequencies versus average $d_{U\text{-}M}$ distances, **Figure S45** (**Supporting Information**). It is worth nothing that the correlations seen in these figures are not strong correlations, and expectedly, the PLS regression analysis for this FIR mode failed to pass the cross-validation and extract any latent variables from the structural parameters, **Figure S46 (Supporting Information**) . When the cross-validation method is bypassed, the PLS model shows complex plane angles and average $d_{U\text{-}M}$ distances are the two most correlated variables with this FIR mode. The failure of the PLS regression analysis to build a statistically relevant model supports the idea that there is weak to no correlations between this FIR mode and the investigated structural parameters.

Finally, the comparisons of $\delta/\rho(UO_4)$ frequencies versus structural DPs revealed that mode stretches are redshifted as DPs values increase, **Figure S47** (**Supporting Information**). In contrast, the qualitative comparison between $\delta/\rho(UO_4)$ mode frequency and counterion eIR revealed a blueshift in this FIR mode as eIR values increased, **Figure 7**, while there was no correlation observed when $\delta/\rho(UO_4)$ mode frequencies and average $d_{U\text{-}M}$ distances were compared, **Figure S47** (**Supporting Information**). Despite the qualitative correlations, the cross-validation tests for PLS models failed to identify a statistically significant factor out of the independent variables. When the cross-validation test was bypassed, complex skew angles and plane angles were the two most correlated variables with this FIR mode, **Figure S48** (**Supporting Information**), yet contributions to mode variance were limited.

Qualitative structural-vibrational comparisons indicated there were correlations between the distortion and structural parameters and FIR modes, and these were quantitatively supplemented using PLS analysis. The PLS regression models for the $\nu(WO_5)_2$ and $\rho(UO_8)$ modes pass cross-validation tests and show that counterion eIR and average $d_{U\text{-}M}$ distances are strongly correlated with these FIR modes. Interestingly, based on these PLS models, structural distortion parameters do not seem to be strongly correlated with FIR modes. When we look at PLS models without the cross-validation test results included, structural DPs do

appear more relevant, but this may be due to overfitting of regression models; thus, no definitive conclusions can be made about the relevance of structural DPs for modulating FIR vibrational modes. Overall, the qualitative and quantitative correlations that we have identified validate and emphasize the importance of the secondary lattice in modulating the FIR properties for complexes **1**-**8**. In particular, the correlations between counterion eIR and average $d_{U\text{-}M}$ distance with the FIR modes demonstrate the importance of counterion identity and size as routes to modulate POM vibrational frequencies.

Moving on to the Raman modes, the POM deformation mode frequencies do not display clear correlation with structural DPs based on qualitative comparisons, **Figure S49** (**Supporting Information**); however, comparisons of POM deformation mode frequencies and counterion eIR and average $d_{U\text{-}M}$ distance do feature linear relationships, **Figures 8** and **S49** (**Supporting Information**). The PLS regression model for the POM deformation modes included two latent variables that account for 50.7% of the variance observed in these Raman modes **Figures S50** and **S51** (**Supporting Information**). Based on the X- and Y-loading plots, counterion eIR is the most strongly correlated parameter with the POM deformation mode frequencies followed by skew angles and average $d_{U\text{-}M}$ distances, **Figure S50** (**Supporting Information**).

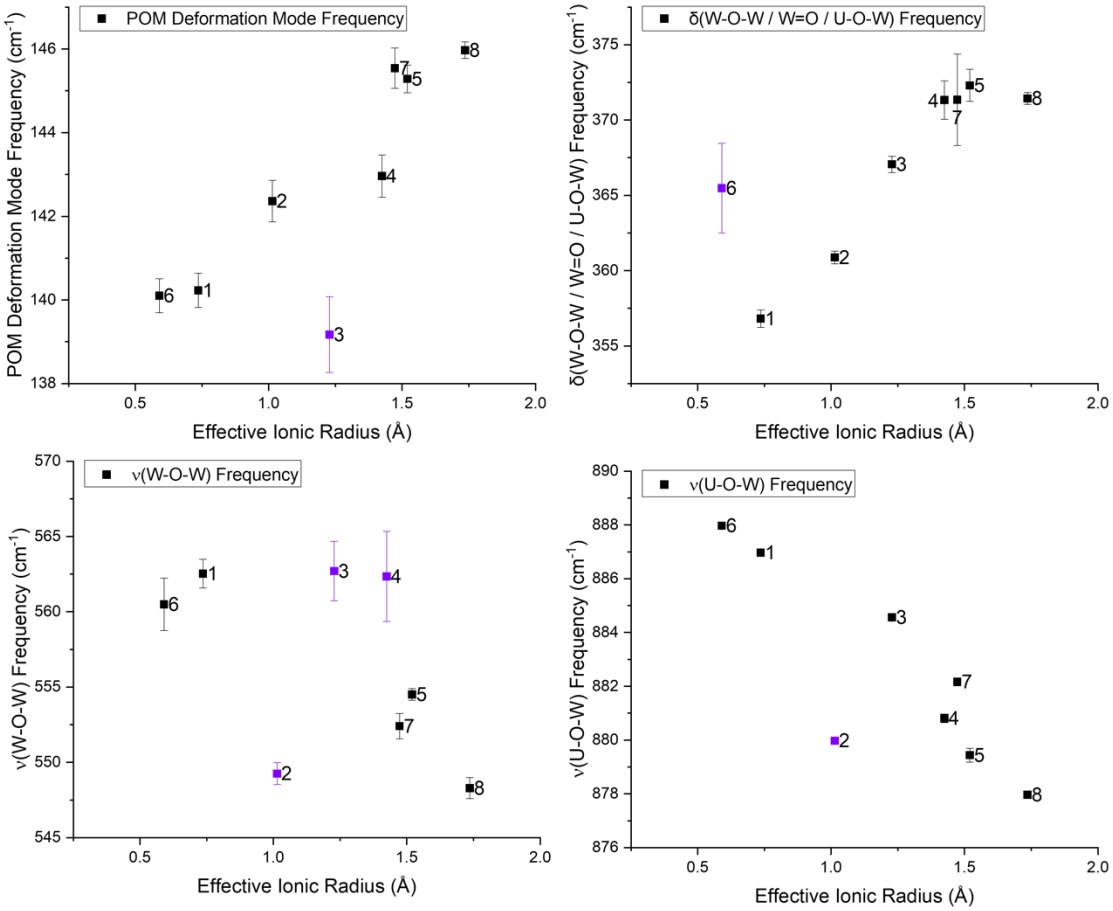

Figure 8. (**Top Left**) Plot of Raman POM deformation mode frequencies vs. counterion eIR values, (**Top Right**) Plot of Raman (W-O-W/W=O/U-O-W) frequencies vs. counterion eIR values, (**Bottom Left**) Plot of Raman ν(W-O-W) frequencies vs. counterion eIR values, and (**Bottom Right**) Plot of Raman ν(U-O-W) frequencies vs. counterion eIR values. Purple data points indicate outliers to observed trends.

Comparisons of δ(W-O-W/W=O/U-O-W) Raman frequencies versus structural DPs do not show any clear correlations, **Figure S52** (**Supporting Information**), and similarly, no clear trend can be observed in the plot comparing δ(W-O-W/W=O/U-O-W) frequencies and average d_{U-M} distances, **Figure S52** (**Supporting Information**). In contrast, we observe a blueshift in δ(W-O-W/W=O/U-O-W) frequencies as the counterion eIR increases (**Figure 8**), and the PLS analysis model for this Raman mode extracted two latent variables that account for 91.0% of the variance in this mode frequency, **Figures S53** and **S54** (**Supporting Information**). Based on the X- and Y-loading plots, **Figure S53** (**Supporting Information**), the structural parameter most correlated with variance in the δ(W-O-W/W=O/U-O-W) stretching frequency is the counterion eIR. The plots comparing ν(W-O-W) Raman frequencies and structural distortion parameters do not show any correlations between these variables, **Figure S55** (**Supporting Information**). Similarly, the plots of ν(W-O-W) Raman frequencies versus counterion eIR values and average d_{U-M} distance do not include any observable correlations, **Figures 8** and **S55** (**Supporting Information**). PLS regression models echo our qualitative observations as none of the structural parameters were found to be statistically valid for modeling ν(W-O-W) Raman frequency variance based on a regression model that includes a cross-validation test, **Figure S56** (**Supporting Information**). When the cross-validation test is bypassed, the resulting PLS model show skew angles and counterion eIR values to be the correlated with the ν(W-O-W) frequencies, **Figure S56** (**Supporting Information**). Finally, the plots comparing ν(U-O-W) Raman frequencies and structural distortion parameters do not show any correlations, **Figure S57** (**Supporting Information**). The comparison of ν(U-O-W) Raman frequencies versus counterion eIR values does display an inverse linear relationship between the two variables with an outlier in complex **2, Figure 8**. This trend is not observed though when comparing (U-O-W) Raman frequencies with average d_{U-M} distances, **Figure S57** (**Supporting Information**). PLS analysis was able to generate a model with two latent variables that accounts for 88.1% of the variance in the ν(U-O-W) frequencies, **Figure S58** and **S59** (**Supporting Information**), and based on the X- and Y-loading plots, **Figure S58** (**Supporting Information**), the ν(U-O-W) frequencies are heavily correlated with counterion eIR values.

Overall, qualitative and PLS analyses show that Raman mode frequencies for complexes **1**-**8** are also modulated by the structural parameters investigated herein. This is especially true for the δ(W-O-W/W=O/U-O-W) and ν(U-O-W) stretches where greater than 80% of the variance in vibrational frequencies for these modes can be accounted for by structural and distortion parameters according to PLS regression analysis. The Raman modes we have focused on display strong correlations with the counterion eIR values, similar to FIR modes, and these results further emphasize the ability of secondary sphere elements to modulate vibrational frequencies. The strong correlations observed between the ν(U-O-W) mode frequency and counterion eIR values demonstrate the vibrational tunability that is offered by changing second sphere counterion as these species can interact with the UO_8 moiety to differing extents, which provides a route for modulating Raman frequencies. The findings here compliment and agree with our previous investigation focused on the $LnW_{10}Na$ Lindqvist POM series.[15] In our recent work, the structural parameters considered were ionic radius of the Ln(III) center and structural distortion parameters (skew angles, plane angles, and plane distances), while the vibrational modes we investigated were the $\nu(WO_5)_2$, $\rho(LnO_8)$, $\nu/\rho(LnO_8)$ modes in the FIR and the δ(W-O-W/W=O/Ln-O-W) and ν(Ln-O-W) modes in Raman spectra.[15] Our results here show that $\rho(UO_8)$, δ(W-O-W/W=O/U-O-W), and ν(U-O-W) vibrational modes are strongly impacted by counterion eIR values, which may explain why the PLS models from our previous investigation were only able to account for 30%, and 51% variance observed for the $\rho(LnO_8)$ and ν(Ln-O-W) stretching frequencies, respectively, and no valid PLS model could be constructed for the δ(W-O-W/W=O/Ln-O-W) Raman mode.[15] Further, our previous study also showed how the $\nu/\rho(LnO_8)$ mode is heavily correlated with complex plane angles, and this matches the results observed here for the $\nu/\rho(UO_8)$ FIR band.[15]

Conclusions

In this study, eight species of U(IV)W_{10} Lindqvist POMs with a range of alkali metal counterions were synthesized and characterized structurally via X-ray diffraction and vibrationally via Raman, MIR, and FIR spectroscopies. This work is the first study to explore U(IV)W_{10} complexes since the initial work from Golubev *et al*. was published nearly fifty years ago,[34] and the crystal structure for $Na_8[UW_{10}]$ (complex **2**) matches what was published by Golubev and colleagues[34] and is also isostructural with Ce(IV) and Th(IV)W_{10} analogues. Changing POM counterions to other alkali metals ranging from Li(I) to Cs(I) facilitated the synthesis of complexes **1**-**8**, which include the first examples of UW_{10} structures with Li(I), K(I), Rb(I), and Cs(I). Complexes **3**-**8** (excluding **6**) include K(I), Rb(I), and Cs(I) as counterions and display increased ion-pairing interactions with the UW_{10} cluster, which agrees with the findings of Colliard and Deblonde as well as Zagrebin *et al*.[18, 48] Specifically, larger counterions (K(I), Rb(I), and Cs(I)) prefer to sit in the belt position surrounding the UW_{10} cluster, which position these counterions close to the first coordination sphere of the U(IV) metal center. Notably, the effective symmetry of the U(IV) center is modulated by the identity and location of the counterions within the lattice, and this was shown through PLS regression analyses which found the counterion eIR and average $d_{U\text{-}M}$ distances could be correlated with changes in structural distortion parameters such as skew and plane angles. These results support our hypothesis that by tuning the secondary sphere around a POM we can modulate the electronic manifolds of the UW_{10} complex to hopefully realize a U(IV) based molecular qubit. The FIR spectra of **1**-**8** show clear distinctions from one another in the form of different major features either being absent or present despite having the same core cluster, and this suggests that some of these modes are likely coupled with lattice phonon modes. In contrast, the Raman spectra of complex **1**-**8** show mostly identical major features for each of the eight UW_{10} complexes described herein. Qualitative and PLS analysis were used to probe the relationship between structural and vibrational properties for complexes **1**-**8**, which revealed significant correlations between counterion eIR values and vibrational modes that indicate the vibrational manifolds of U(IV)W_{10} complexes can be tuned via modulation of the composition and packing of secondary sphere elements. The strong correlations between vibrational modes involving the UO_8 moiety with counterion eIR values and average $d_{U\text{-}M}$ distances suggests the extent of interactions between the UW_{10} cluster and the lattice counterions is driven by the size and location of the ions relative to the cluster, and these results provide the foundation to vastly expand the electronic tunability of Ln and An POM complexes due to the endless combination of secondary sphere elements that can be included with POM clusters. We are currently pursuing magnetic and electron paramagnetic resonance measurements to directly probe the electronic ground states and spin-properties of the UW_{10} species, and overall, this study has clearly demonstrated the importance of secondary sphere elements on the structural and vibrational manifolds of Lindqvist POM complexes. U(IV) chemistry is also an ideal platform for extending research efforts to other tetravalent actinides, and studies with Pu(IV) are underway.

Supporting Information Available

Supporting data includes MIR spectra of the tungstate starting materials, structural figures for complexes **1**-**8**, crystallographic parameters for polymorph **1b**, tables of interatomic distances for complexes **1**-**8**, and methodological details for determining structural distortion parameters, counterion eIR, and average $d_{U\text{-}M}$ distances for complexes **1**-**8**. Methodological specifics for the PLS regression models, raw and fitted FIR and Raman spectra for complexes **1**-**8**, plots comparing FIR and Raman vibrational modes frequencies and structural parameters, as well as plots produced by PLS analysis where the relationship between FIR and Raman vibrational modes frequencies and structural distortion parameters were investigated are included as well. The CIFs for complexes **1**-**8** have also been deposited at the Cambridge Crystallographic Database Centre and may be obtained from http://www.ccdc.cam.ac.uk by citing reference numbers 2381891-2381898.

Author Information

Corresponding Author

*E-mail: korey-carter@uiowa.edu

Notes

The authors declare no competing interests.

Acknowledgements

This work was supported by the U.S. Department of Energy, Office of Science, Office of Basic Energy Sciences, Early Career Research Program under Award DE-SC0024035. We acknowledge the University of Iowa Materials, Analysis, Testing, and Fabrication Facility for use of single crystal and powder X-ray diffractometers as well as the Raman microscope used in this study. Single crystal XRD data was collected on an instrument funded by NSF Award CHE-1828117. Mid- and far-IR spectra were collected on an instrument funded by a Nuclear Regulatory Commission Faculty Development Grant (NRC 31310018M0042).

References

(1) Errington, R. Rational approaches to polyoxometalate synthesis. In *Polyoxometalate Chemistry From Topology via Self-Assembly to Applications*, Pope, M. T., Müller A. Eds.; Springer, Dordrecht, **2001**, pp. 7-22.
(2) *Polyoxometalate Molecular Science*, Borrás-Almenar, J. J., Coronado, E., Müller, A., Pope, M. Eds.; Springer, Dordrecht **2003**.
(3) Liu, J.-C.; Zhao, J.-W.; Streb, C.; Song, Y.-F. Recent advances on high-nuclear polyoxometalate clusters. *Coordination Chemistry Reviews* **2022**, *471*, 214734.
(4) Song, Y.-F.; Tsunashima, R. Recent advances on polyoxometalate-based molecular and composite materials. *Chemical Society Reviews* **2012**, *41*, 7384-7402.
(5) Khalilpour, H.; Shafiee, P.; Darbandi, A.; Yusuf, M.; Mahmoudi, S.; Goudarzi, Z. M.; Mirzamohammadi, S. Application of Polyoxometalate-based composites for sensor systems: A review. *Journal of Composites and Compounds* **2021**, *3*, 129-139.
(6) Zhang, Y.; Liu, J.; Li, S.-L.; Su, Z.-M.; Lan, Y.-Q. Polyoxometalate-based materials for sustainable and clean energy conversion and storage. *EnergyChem* **2019**, *1*, 100021.
(7) Bijelic, A.; Aureliano, M.; Rompel, A. Polyoxometalates as potential next-generation metallodrugs in the combat against cancer. *Angewandte Chemie International Edition* **2019**, *58*, 2980-2999.
(8) Baldoví, J.; Cardona-Serra, S.; Gaita-Ariño, A.; Coronado, E. Design of Magnetic Polyoxometalates for Molecular Spintronics and as Spin Qubits. In *Advances in Inorganic Chemistry*, van Eldik, R.; Cronin, L. Eds.; Vol. 69; Elsevier, **2017**; pp 213-249.
(9) Ammam, M. Polyoxometalates: formation, structures, principal properties, main deposition methods and application in sensing. *Journal of Materials Chemistry A* **2013**, *1*, 6291-6312.
(10) Boskovic, C. Rare earth polyoxometalates. *Accounts of Chemical Research* **2017**, *50*, 2205-2214.
(11) An, H.; Han, Z.; Xu, T. Three-dimensional architectures based on lanthanide-substituted double-Keggin-type polyoxometalates and lanthanide cations or lanthanide-organic complexes. *Inorganic Chemistry* **2010**, *49*, 11403-11414.
(12) AlDamen, M. A.; Cardona-Serra, S.; Clemente-Juan, J. M.; Coronado, E.; Gaita-Arino, A.; Marti-Gastaldo, C.; Luis, F.; Montero, O. Mononuclear lanthanide single molecule magnets based on the polyoxometalates $[Ln(W_5O_{18})_2]^{9-}$ and $[Ln(\beta_2\text{-}SiW_{11}O_{39})_2]^{13-}$ (Ln^{III}= Tb, Dy, Ho, Er, Tm, and Yb). *Inorganic Chemistry* **2009**, *48*, 3467-3479.

(13) Bassil, B. S.; Dickman, M. H.; von der Kammer, B.; Kortz, U. The Monolanthanide-Containing Silicotungstates $[Ln(\beta_2\text{-}SiW_{11}O_{39})_2]^{13-}$ (Ln= La, Ce, Sm, Eu, Gd, Tb, Yb, Lu): A Synthetic and Structural Investigation. *Inorganic Chemistry* **2007**, *46*, 2452-2458.
(14) Peacock, R.; Weakley, T. Heteropolytungstate complexes of the lanthanide elements. Part I. Preparation and reactions. *Journal of the Chemical Society A: Inorganic, Physical, Theoretical* **1971**, 1836-1839.
(15) Subintoro, P. J.; Carter, K. P. Structural and vibrational properties of lanthanide Lindqvist polyoxometalate complexes. *Dalton Transactions* **2024**, *53*, 9526-9539.
(16) Colliard, I.; Lee, J. R.; Colla, C. A.; Mason, H. E.; Sawvel, A. M.; Zavarin, M.; Nyman, M.; Deblonde, G. J.-P. Polyoxometalates as ligands to synthesize, isolate and characterize compounds of rare isotopes on the microgram scale. *Nature Chemistry* **2022**, *14*, 1357-1366.
(17) Colliard, I.; Deblonde, G. J.-P. Characterization of the first Peacock–Weakley polyoxometalate containing a transplutonium element: curium bis-pentatungstate $[Cm(W_5O_{18})_2]^{9-}$. *Chemical Communications* **2024**, *60*, 5999-6002.
(18) Colliard, I.; Deblonde, G. J.-P. Polyoxometalate Ligands Reveal Different Coordination Chemistries Among Lanthanides and Heavy Actinides. *JACS Au* **2024**, *4*, 2503-2513.
(19) Yang, G.-P.; Li, K.; Hu, C.-W. Recent advances in uranium-containing polyoxometalates. *Inorganic Chemistry Frontiers* **2022**, *9*, 5408-5433.
(20) Auvray, T.; Matson, E. M. Polyoxometalate-based complexes as ligands for the study of actinide chemistry. *Dalton Transactions* **2020**, *49*, 13917-13927.
(21) Pope, M. T. Structural chemistry of actinide polyoxometalates. In *Structural Chemistry of Inorganic Actinide Compounds*, Krivovichev, S. V., Burns, P. C., Tananaev, I. G. Eds.; Elsevier, **2007**; pp 341-361.
(22) Shiels, D.; Brennessel, W. W.; Crawley, M. R.; Matson, E. M. Leveraging a reduced polyoxomolybdate-alkoxide cluster for the formation of a stable U(V) sandwich complex. *Chemical Science* **2024**, *15*, 11072-11083.
(23) Valerio, L. R.; Shiels, D.; Lopez, L. M.; Mitchell, A. W.; Zeller, M.; Bart, S. C.; Matson, E. M. Venturing Past Uranium: Synthesis of a Np(IV) Polyoxomolybdate–Alkoxide Sandwich Complex. *Inorganic Chemistry* **2024**, *63*, 22639-22649.
(24) Pope, M. T. *Polyoxometalates for radioactive waste treatment*; U. S. Department of Energy, Office of Environmental Management, Washington, DC, USA **1998**.
(25) Liu, M.; Peng, X.-H.; Guo, F.-S.; Tong, M.-L. Actinide-based single-molecule magnets: alone or in a group? *Inorganic Chemistry Frontiers* **2023**, *10*, 3742-3755.
(26) Spivak, M.; Vogiatzis, K. D.; Cramer, C. J.; de Graaf, C.; Gagliardi, L. Quantum chemical characterization of single molecule magnets based on uranium. *The Journal of Physical Chemistry A* **2017**, *121*, 1726-1733.
(27) Liddle, S. T.; van Slageren, J. Actinide Single-Molecule Magnets. In *Lanthanides and Actinides in Molecular Magnetism*, Layfield, R. A., Murugesu, M. Eds.; Wiley-VCH, Weinheim, **2015**, pp. 315-340.
(28) Baldoví, J. J.; Gaita-Ariño, A.; Coronado, E. Modeling the magnetic properties of lanthanide complexes: relationship of the REC parameters with Pauling electronegativity and coordination number. *Dalton Transactions* **2015**, *44*, 12535-12538.
(29) Gaita-Ariño, A.; Luis, F.; Hill, S.; Coronado, E. Molecular spins for quantum computation. *Nature Chemistry* **2019**, *11*, 301-309.
(30) Aromí, G.; Roubeau, O. Lanthanide molecules for spin-based quantum technologies. In *Handbook on the Physics and Chemistry of Rare Earths*, Bünzli, J.-C. G., Pecharsky, V. K. Eds.; Vol. 56; Elsevier, **2019**; pp 1-54.
(31) Zadrozny, J. M.; Niklas, J.; Poluektov, O. G.; Freedman, D. E. Millisecond coherence time in a tunable molecular electronic spin qubit. *ACS Central Science* **2015**, *1*, 488-492.
(32) Baldoví, J. J.; Cardona-Serra, S.; Clemente-Juan, J. M.; Coronado, E.; Gaita-Ariño, A. Modeling the properties of uranium-based single ion magnets. *Chemical Science* **2013**, *4*, 938-946.
(33) Shiddiq, M.; Komijani, D.; Duan, Y.; Gaita-Ariño, A.; Coronado, E.; Hill, S. Enhancing coherence in molecular spin qubits via atomic clock transitions. *Nature* **2016**, *531*, 348-351.

(34) Golubev, A.; Kazanskii, L.; Torchenkova, E.; Simonov, V.; Spitsyn, V. Crystal structure of sodium decatungstenuranate (4).[$Na_8UW_{10}O_{36}$•$30H_2O$]. *Doklady Akademil Nauk SSSR* **1975,** *221*, 351-352.
(35) Patel, D.; Wooles, A. J.; Hashem, E.; Omorodion, H.; Baker, R. J.; Liddle, S. T. Comments on reactions of oxide derivatives of uranium with hexachloropropene to give UCl_4. *New Journal of Chemistry* **2015**, *39*, 7559-7562.
(36) Hermann, J. A.; Suttle, J. F.; Hoekstra, H. R. *Uranium (IV) Chloride*. In *Inorganic Syntheses*, Moeller, T. Ed.; Vol. 5; McGraw-Hill Book Company, **1957**, pp. 143-145.
(37) Mariichak, O. Y.; Ignatyeva, V.; Baumer, V.; Rozantsev, G.; Radio, S. Heteropoly Decatungstolanthanidates (III) with Peacock–Weakley Type Anion: Synthesis and Crystal Structure of Isostructural Salts $Na_9[Ln(W_5O_{18})_2]$•$35H_2O$ (Ln= Gd, Er). *Journal of Chemical Crystallography* **2020**, *50*, 255-266.
(38) APEX4, Bruker AXS Inc., Madison, WI, USA, 2022.
(39) Krause, L.; Herbst-Irmer, R.; Sheldrick, G. M.; Stalke, D. Comparison of silver and molybdenum microfocus X-ray sources for single-crystal structure determination. *Journal of applied crystallography* **2015**, *48*, 3-10.
(40) Sheldrick, G. M. SHELXT–Integrated space-group and crystal-structure determination. *Acta Crystallographica Section A: Foundations and Advances* **2015**, *71*, 3-8.
(41) Sheldrick, G. M. Crystal structure refinement with SHELXL. *Acta Crystallographica Section C: Structural Chemistry* **2015**, *71*, 3-8.
(42) Palmer, D. CrystalMaker, CrystalMaker Software Ltd, Begbroke, Oxfordshire, England, 2014.
(43) OriginPro, Version 2024, Origin Lab Corporation, Northampton, MA, USA.
(44) Kumar, G. A.; Shruthi, D. The nature of the chemical bond in sodium tungstate based on ab initio, DFT and QTAIM topological analysis of electron density. *Materials Today: Proceedings* **2021**, *44*, 3127-3132.
(45) Shiozaki, R.; Inagaki, A.; Nishino, A.; Nishio, E.; Maekawa, M.; Kominami, H.; Kera, Y. Spectroscopic investigation of a series of sodium lanthanide decatungstates, $Na_7H_2Ln(III)(W_5O_{18})_2$•$nH_2O$ (Ln: La-Yb): the contribution of 4fn electrons to bonding interaction among Ln (III) and polyoxotungstates. *Journal of Alloys and Compounds* **1996**, *234*, 193-198.
(46) Rocchiccioli-Deltcheff, C.; Thouvenot, R.; Fouassier, M. Vibrational investigations of polyoxometallates. 1. Valence force field of $Mo_6O_{19}^{2-}$ based on total isotopic substitution (^{18}O, ^{92}Mo, ^{100}Mo). *Inorganic Chemistry* **1982**, *21*, 30-35.
(47) Kazanskii, L.; Golubev, A.; Baburina, I.; Torchenkova, E.; Spitsyn, V. Vibration spectra of $XW_{10}O_{36}^{n-}$ heteropolyanions. *Bulletin of the Academy of Sciences of the USSR, Division of Chemical Science* **1978**, *27*, 1956-1960.
(48) Zagrebin, P. A.; Nazmutdinov, R. R.; Spector, E. A.; Borzenko, M. I.; Tsirlina, G. A.; Mikhelson, K. N. Ionic association of Ce (IV)-decatungstate in the context of heteroatom reduction. *Electrochimica Acta* **2010**, *55*, 6064-6072.
(49) Gagné, O. C.; Hawthorne, F. C. Bond-length distributions for ions bonded to oxygen: alkali and alkaline-earth metals. *Acta Crystallographica Section B: Structural Science, Crystal Engineering and Materials* **2016**, *72*, 602-625.
(50) Shannon, R. D. Revised effective ionic radii and systematic studies of interatomic distances in halides and chalcogenides. *Acta Crystallographica Section A: Crystal Physics, Diffraction, Theoretical and General Crystallography* **1976**, *32*, 751-767.
(51) Blockmon, A. L.; Ullah, A.; Hughey, K. D.; Duan, Y.; O'Neal, K. R.; Ozerov, M.; Baldoví, J. J.; Aragó, J.; Gaita-Ariño, A.; Coronado, E. Spectroscopic analysis of vibronic relaxation pathways in molecular spin qubit $[Ho(W_5O_{18})_2]^{9-}$: sparse spectra are key. *Inorganic Chemistry* **2021**, *60*, 14096-14104.

For Table of Contents Only

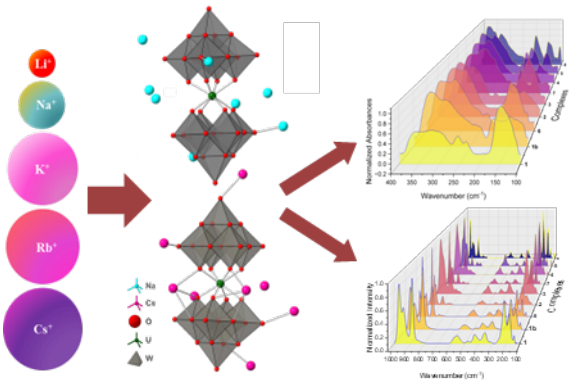

The structural and vibrational properties of eight U(IV) Lindqvist (UW_{10}) polyoxometalates featuring a range of alkali metal counterions were investigated to ascertain how changes in second sphere packing and interactions impact the structural and vibrational manifolds relevant to spin based relaxation processes.